Adaptive Boundary Control Using Natural Switching Surfaces for Flyback Converters Operating in the Boundary Conduction Mode with Parameter Uncertainties

Luciano Andrés Garcia Rodriguez, *Student Member, IEEE*, Héctor Gerardo Chiacchiarini, David Carballo Rojas, *Student Member, IEEE*, and Juan Carlos Balda, *Senior Member, IEEE*

***Abstract*—The derivation and implementation of the natural switching surfaces (NSS) considering certain parametric uncertainties for a flyback converter operating in the boundary conduction mode is the main focus of this paper. The NSS with nominal parameters presents many benefits for the control of nonlinear systems; for example, fast transient response under load-changing conditions. However, the performance worsens considerably when the converter actual parameters are different from the ones used in the design process. Therefore, a novel control strategy for NSS considering the effects of parameter uncertainties is proposed. This control law can estimate and adapt the control trajectories in a minimum number of switching cycles to obtain excellent performances even under extreme parameter uncertainties. The analytical derivation of the proposed adaptive switching surfaces is presented together with simulations and experimental results showing adequate performance under different tests, including comparisons with a standard PI controller.**

***Index Terms*—Adaptive controller, boundary conduction mode (BCM), boundary control (BC), critical conduction mode (CRM), flyback converter, natural switching surface (NSS), nonlinear control, parametric uncertainties, switching surface control (SSC), variable structure control (VSC).**

I. INTRODUCTION

THE flyback converter is one of the most commonly used topologies in systems rated up to 200 W due to many benefits such as low part count, low cost, electrical isolation, and wide voltage ratio [1]. In addition to the traditional applications

Manuscript received April 10, 2018; revised August 17, 2018; accepted October 15, 2018. Date of publication October 30, 2018; date of current version May 22, 2019. This work was supported in part by the University of Arkansas, USA, and in part by the CONICET and Universidad Nacional del Sur from Argentina. Recommended for publication by Associate Editor M. Ordonez. *(Corresponding author: Luciano Andrés Garcia Rodriguez.)*

L. A. Garcia Rodriguez, D. Carballo Rojas, and J. C. Balda are with the Department of Electrical Engineering, University of Arkansas, Fayetteville, AR 72701 USA (e-mail:

dependent on the load and supply characteristics which reduce the overall system performance [10]. An ideal SS is the one that guides the system to the desired steady state with the minimum number of switching actions [14]. The ideal SS is derived from the intersection of the system OFF trajectory that contains the operating point with the ON trajectory that leaves the operating point [12]–[14].

Multiple SS have been proposed to estimate the ideal trajectories or natural response of converters. For example, second-order SS derived from capacitor charge-balance equations with low ripple approximation have been proposed for buck converters operating in CCM [18] and DCM [20]. Also, a fixed-frequency second-order SS using a variable-width hysteresis loop was presented in [21]. A similar methodology was applied to single-phase [22]–[23] and three-phase inverters [24]. Other types of second-order SS derived using the state-energy plane were proposed for single- and dual-output boost converters [10], [25]. Higher order SS for inverters were derived in [19] and [26], where logarithmic SS were used to approximate the system trajectories. Another method to approximate the ideal trajectories was derived from the converter differential equations assuming a constant-current load [27]. Using those SS called the natural switching surfaces (NSS) warrants no output voltage overshoot for a step load variation under nominal design conditions, excellent response for any change of the load resistance, and much easier trajectory derivation because of the absence of the exponential decay, spirals, or hyperbolic terms related to the presence of the load resistance in the differential equations [13]. This method was first presented in [27] for buck converters and then extended to the inverters [28], boost [11], [29], buck–boost [30], dual active bridge [31], full bridge [32], and flyback converters [33], [34].

The main drawback of BC is the dependence of the SS on the converter parameters [12], [14], which are exposed to changes due to tolerance, aging effect, humidity, and temperature [23], [24]. Parameter variations impact on the steady-state performance [19], [20] and lead to stability issues because of changes on the shape of the SS [29] and converter operating modes [10]. This paper presents a solution to those issues by deriving the NSS and the control law for a flyback converter operating in BCM and considering parameter uncertainties. The proposed control law can provide a very precise estimation of the parameter variations in only a single switching action and then continuously adapt the control SS before a new switching action occurs. Therefore, the converter can reach the steady-state operation in a single switching action for sudden load changes even under extreme converter parameter variations.

This paper is organized as follows. The normalized system trajectories considering parametric uncertainties are derived in Section II. Then, the start-up and steady-state characteristics are presented in Section III. The adaptive control laws are developed in Section IV. The design procedure and an example are given in Section V. The feasibility of the proposed control law is validated through simulation results in Section VI and experimental results in Section VII. Finally, Section VIII presents the conclusions.

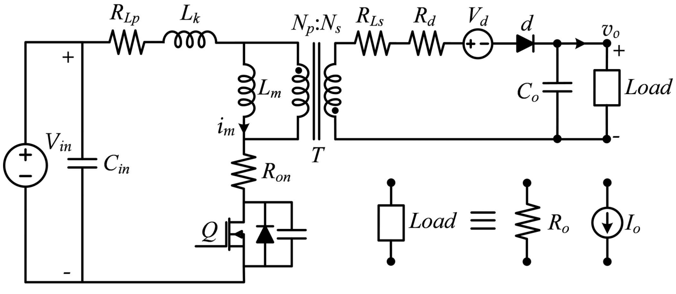

Fig. 1. Flyback converter with parasitic elements.

II. Derivation of Normalized System Trajectories Considering Parametric Uncertainties

The circuit shown in Fig. 1 represents a flyback converter either for resistive load R_o or for constant-current load I_o. It includes the following circuit and parasitic elements.

1) Q: Transistor.
2) d: Diode.
3) T: Transformer.
4) $n = N_p/N_s$: Transformer turns ratio.
5) L_m: Transformer magnetizing inductance.
6) L_k: Transformer leakage inductance.
7) C_{in}: Input capacitor.
8) C_o: Output capacitor.
9) R_{Lp}: Primary-side winding resistance.
10) R_{ON}: Switch ON resistance.
11) $R_p = R_{Lp} + R_{ON}$: Total primary resistance.
12) R_d: Diode ON resistance.
13) R_{Ls}: Secondary-side winding resistance.
14) $R_s = R_d + R_{Ls}$: Total secondary resistance.
15) V_d: Diode forward voltage drop.

The stationary and transient responses of the circuit for both load conditions can be obtained from the circuit equations. For the case of a resistive load, after some basic calculations, the following steady-state solution can be obtained:

$$(V_{in} - I_m R_p)\, D = n\,(V_o + V_d + nI_m R_s)\,(1 - D) \quad (1)$$

$$I_m n\,(1 - D) = V_o/R_o. \quad (2)$$

By solving for the duty cycle D from (2) and replacing it in (1), the flyback converter load line for a resistive load is given by

$$I_m R_p R_o + \frac{V_o}{I_m}\left(V_o + \frac{V_{in}}{n} + V_d\right) = V_o\left(\frac{R_p}{n} - nR_s\right) + V_{in}R_o. \quad (3)$$

Fig. 2(a) shows the load line from (3), and ON and OFF-BCM flyback trajectories obtained by solving the circuit equations for the ON- and OFF-switch states for different arbitrary initial conditions. The load resistor R_o is 48 Ω and the input voltage source V_{in} is 6 V. The value of the parasitic elements of the flyback components are shown in Table I and they represent the same actual parameters from the components used for the simulation and experimental results included in this study.

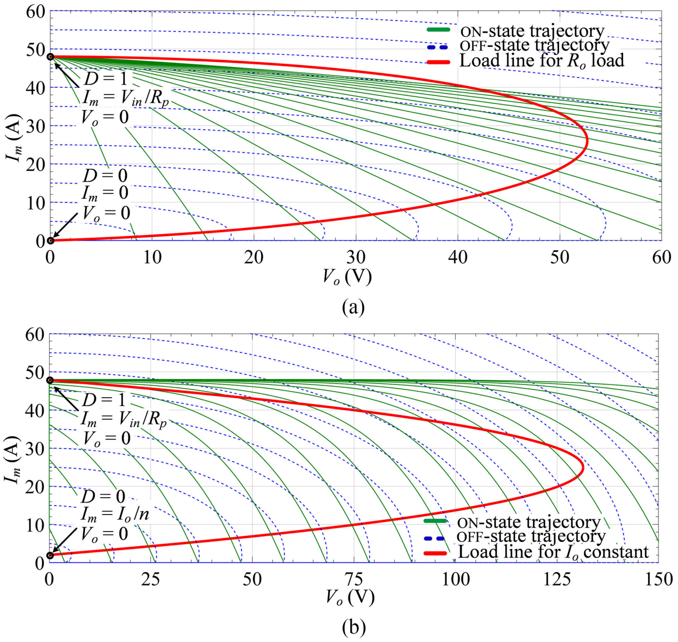

(a)

(b)

Fig. 2. Load line for a flyback converter with (a) a resistive load and (b) a constant-current load.

TABLE I
FLYBACK CONVERTER PARASITIC ELEMENTS

Component	Parasitic Element	Value
Transformer	L_k	1.58 µH
	R_{Lp}	0.048 Ω
	R_{Ls}	0.110 Ω
Transistor	R_{ON}	0.077 Ω
Diode	V_d	0.58 V
	R_d	0.02 Ω

For the constant-current load, the following steady-state solution can be derived after some basic calculations

$$(V_{in} - I_m R_p)\, D = n\,(1 - D)\,(V_o + V_d + nI_m R_s) \quad (4)$$

$$I_o = n\,(1 - D)\, I_m . \quad (5)$$

By solving for the duty cycle D from (5) and replacing it into (4), the load line for a flyback with constant-current load is obtained as

$$I_m R_p + \frac{I_o}{I_m}\left(\frac{V_{in}}{n} + V_o + V_d\right) = I_o\left(\frac{R_p}{n} - nR_s\right) + V_{in} . \quad (6)$$

Fig. 2(b) shows the load line for a constant-current load and the ON and OFF trajectories when the actual converter parameters from Table I are used. The constant-current load I_o was set to 0.5 A and the input voltage to $V_{in} = 6$ V.

The load lines considering parasitic components derived for the resistive and constant-current load cases are compared below to the load lines obtained without parasitic components to show that the ideal model and the model considering parasitic elements behave very similarly under steady-state conditions. The ideal load line for the resistive load case is obtained by making the parasitic elements equal to zero on (3) as

$$V_o^2 n + V_o V_{in} = I_m V_{in} R_o n . \quad (7)$$

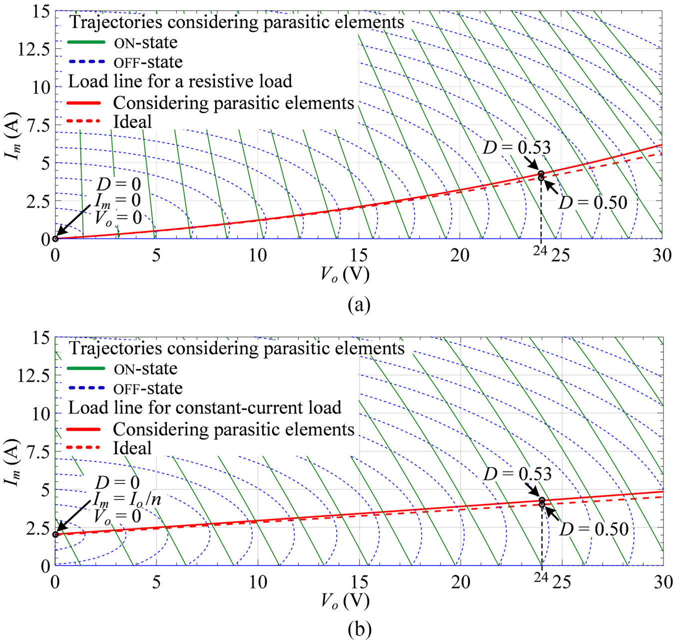

(a)

(b)

Fig. 3. Actual and ideal flyback converter load lines for (a) a resistive load, and (b) a constant-current load.

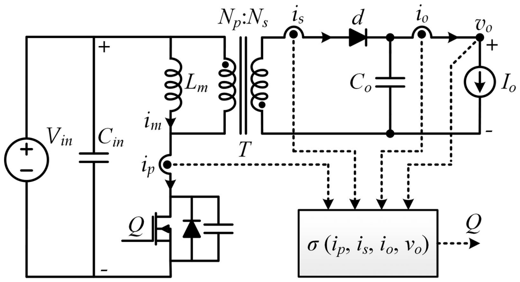

Fig. 4. Flyback converter circuit including current and voltage sensors.

Fig. 3(a) shows the ideal and real load lines, and the ON- and OFF-real BCM trajectories. It is possible to see that they are very similar during most of the operating range. If the particular case with $V_o = 24$ V, $V_{in} = 6$ V, and the turns ratio $N_p/N_s = 1/4$ is considered, the ideal duty cycle D is 0.5. However, D should be 0.53 under conditions with actual parameters, which represents a 6% of duty cycle variation.

The actual and the ideal flyback load lines for the case of a constant-current load are shown in Fig. 3(b). Like the case of a resistive load, the actual and ideal load lines for a constant-current load are similar for the duty cycle range ($0 < D < 0.8$). For example, if $V_o = 24$ V, $V_{in} = 6$ V, and the turns ratio $N_p/N_s = 1/4$ is considered, the ideal duty cycle D is 0.5, while $D = 0.53$ is needed when actual components are used.

It is concluded that flyback circuits with typical parasitic components can be analyzed under ideal conditions (no parasitic components) without producing relevant errors.

The system shown in Fig. 4 is a simplified version of a flyback converter which consists of an ideal transistor Q, and ideal diode *d*, flyback transformer *T* with magnetizing inductance L_m, as well as input and output capacitors C_{in} and C_o. These parameters are the converter actual parameters which may differ from the nominal ones used in the design process. The components which determine the dynamics of a flyback converter are the magnetizing inductance and output capacitance [33]. The nominal output capacitance is $\bar{C}_o$ and the nominal magnetizing inductance is $\bar{L}_m$. The load is represented by a constant-current load which states the worst-case scenario in terms of stability [11]. The normalization of the system consists of a scale change of variables on its differential equations which enables a general solution [27]. The presence of a transformer makes it necessary to relate the converter parameters to one side; the secondary side is selected in this case. The normalization is performed using the nominal output voltage as the reference voltage $V_r = v_o$, the characteristic nominal impedance of the combined nominal magnetizing inductance referred to the secondary side and the nominal output capacitor, $\bar{Z}_o = (1/n)\sqrt{\bar{L}_m/\bar{C}_o}$ as the reference impedance Z_r and the natural frequency $\bar{f}_o = n/(2\pi\sqrt{\bar{L}_m\bar{C}_o})$ as the reference frequency f_r. The normalizing equations of the voltage, current, and time variables as well as their derivatives for the secondary variables are as follows:

$$v_n = v/V_r, \qquad dv_n = dv/V_r \tag{8}$$

$$i_n = i \cdot Z_r/V_r, \quad di_n = di \cdot Z_r/V_r \tag{9}$$

$$t_n = t \cdot f_r, \qquad dt_n = dt \cdot f_r \tag{10}$$

where *v*, *i*, and *t* are the standard voltage, current, and time variables of the secondary side, and v_n, i_n, and t_n are their normalized versions. The normalizing equations must be reflected back to the primary side to normalize primary variables as follows:

$$v_n = v/\left(n \cdot V_r\right), \quad i_n = i \cdot n \cdot Z_r/V_r \tag{11}$$

$$dv_n = dv/\left(n \cdot V_r\right), \quad di_n = di \cdot n \cdot Z_r/V_r. \tag{12}$$

The next sections present the derivation of the normalized OFF- and ON-state general natural trajectories on the plane i_{mn} versus v_{on}, which depend on generic initial conditions, input voltage, and output current. Later, specific natural trajectories containing the point $i_{mn} = 0$, $v_{on} = V_{TPn}$ will be analyzed. This specific point characterizes the operation in BCM. As will be explained in the sequel, voltage V_{TPn} is set as the desired target point voltage which leads to the converter producing the required root-mean-square (RMS) value of the voltage output.

A. OFF-State Trajectory

Diode *d* conducts during the OFF state of transistor *Q* and the energy stored in the transformer during the ON state is transferred to the load. The voltage applied to the magnetizing inductance is the output voltage multiplied by the transformer turns ratio. The following expressions are the differential equations that describe this mode of operation, where L_m and C_o are the actual parameters of the converter

$$L_m \frac{di_m}{dt} = -nv_o \tag{13}$$

$$C_o \frac{dv_o}{dt} = ni_m - i_o. \tag{14}$$

Using (8) through (12), the normalization of (13) and (14) becomes

$$\frac{di_{mn}}{dt_n} = -2\pi \frac{\overline{L}_m}{L_m} v_{on} \tag{15}$$

$$\frac{dv_{on}}{dt_n} = 2\pi \frac{\overline{C}_o}{C_o}\left(i_{mn} - i_{on}\right). \tag{16}$$

Differentiating both sides of (15) and replacing it in (16) yields a differential equation with the following solution:

$$i_{mn}\left(t_n\right) = i_{on} + A\cos\left(2\pi\sqrt{\alpha\beta}t_n\right) + B\sin\left(2\pi\sqrt{\alpha\beta}t_n\right) \tag{17}$$

where $\alpha = \bar{L}_m/L_m$, $\beta = \bar{C}_o/C_o$, $A = i_{mn}(0^-) - i_{on}$, and $B = \frac{1}{2\pi\sqrt{\alpha\beta}}\frac{di_{mn}(0^-)}{dt_n}$. By applying the trigonometric property $A\cos(x) + B\sin(x) = \sqrt{A^2+B^2}\sin(x + \tan^{-1}(A/B))$ to (17), taking the derivative of the resulting expression and using the property $\cos(\sin^{-1}(x)) = \sqrt{1-x^2}$, the result is an equation that does not depend on the normalized time. Then, the OFF-state trajectory can be expressed as follows:

$$\lambda_{OFF} := v_{on}^2\frac{\alpha}{\beta} + \left(i_{mn} - i_{on}\right)^2 - A^2 - B^2 = 0. \tag{18}$$

Therefore, in the case where the nominal parameters are the same as the actual ones ($\alpha/\beta = 1$), λ_{OFF} is a circle with its center at $(i_{mn}, v_{on}) = (i_{on}, 0)$ and a radius that is a function of the specifications of the converter [33]. However, λ_{OFF} becomes an ellipse in the case where the actual parameters differ from those used in the design process.

B. ON-State Trajectory

The magnetizing inductance is connected to the input source and the diode in the secondary side is reversed bias when the transistor *Q* is ON. The differential equations for this stage and their normalized versions are

$$v_{in} = L_m\frac{di_m}{dt} \tag{19}$$

$$-i_o = C_o\frac{dv_o}{dt} \tag{20}$$

$$2\pi\alpha v_{inn} = \frac{di_{mn}}{dt_n} \tag{21}$$

$$-2\pi\beta i_{on} = \frac{dv_{on}}{dt_n}. \tag{22}$$

From (21) and (22), when *Q* is ON, the normalized magnetizing current and output voltage vary linearly with time. Dividing these two normalized equations yield

$$\frac{di_{mn}}{dv_{on}} = -\frac{\alpha}{\beta}\frac{v_{inn}}{i_{on}}. \tag{23}$$

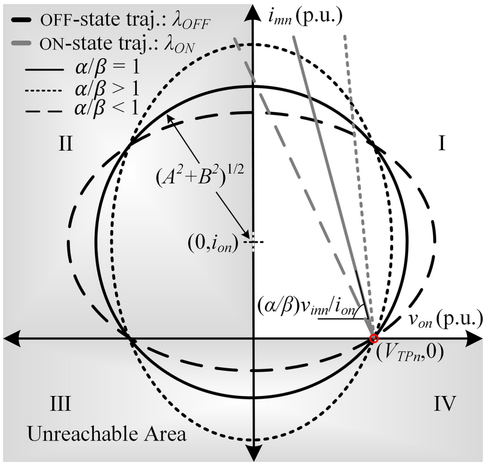

Fig. 5. Normalized natural surfaces for a flyback converter operating in BCM under parametric uncertainties.

By integrating (23), the natural trajectory of the flyback converter when the transistor Q is ON is given by

$$\lambda_{ON} := i_{mn} + \frac{\alpha}{\beta}\frac{v_{inn}}{i_{on}}v_{on} - H = 0 \tag{24}$$

where H is a constant that depends on the initial conditions selected for starting the ON state. In particular, if the initial conditions for the λ_{OFF} trajectory are properly imposed (i.e., designing the controller adequately), the natural OFF-trajectory will intersect the state-space target point $(0, v_{on})$, and H in λ_{ON} can also be selected such that λ_{ON} intersects the same target point.

The loci λ_{OFF} and λ_{ON} are the natural trajectories of the system when the switch is OFF and ON, respectively. Those natural trajectories start from the initial conditions which correspond to the time instants when the switch commutes. By properly selecting the switching times, specific natural trajectories can be selected to be the NSS that lead the converter to the target operating condition.

C. Graphical Analysis of the NSS Trajectories with Parametric Uncertainties

Fig. 5 presents the graphical renditions of the NSS trajectories previously derived. These graphs show different elliptic trajectories λ_{OFF} all passing through the point $(V_{TPn}, 0)$ for the BCM operation presented in the next section. As previously described, λ_{ON} is a descending sloping line and λ_{OFF} is a circle with a center at $(0, i_{on})$ for the case when $\alpha/\beta = 1$ and an ellipse for the case when $\alpha/\beta \neq 1$. This section shows the interaction of the two trajectories and their relationship with the converter operation.

Analyzing the operation of the flyback converter on the i_{mn} versus v_{on} plane, quadrants of the plane can immediately be recognized as unobtainable or undesirable operation zones based on the polarity of the variables. For example, i_{mn} must be positive for the flyback converter to operate correctly. Therefore, i_{mn} would not be attainable in quadrants III or IV. Likewise, the converter could not operate if v_{on} was negative. If the converter was operating when v_{on} were negative, it would imply that the load would be transferring power to the input of the converter, which is physically impossible due to the presence of the diode d. Therefore, v_{on} should not operate in quadrants II or III. This leaves quadrant I as the only operational quadrant that satisfies the constraints for both variables. In quadrant I, i_{mn} and v_{on} are both positive and the flyback converter would be transferring power to the load. The unreachable quadrants have been grayed out in Fig. 5.

If the converter's trajectories were to reach an axis, the converter would then evolve on that axis. Therefore, the converter upon reaching the i_{mn} axis would change i_{mn}, while the output voltage remained at zero. Likewise, the converter upon reaching the v_{on} axis would change v_{on}, while keeping the magnetizing current at zero. This is due to the unobtainable quadrants.

D. Selection of the Target Point for Operation in BCM

The free parameters of λ_{ON} and λ_{OFF} in (18) and (24) should be selected for the natural trajectories to contain a target operating point that maintains the converter operating in BCM for all loading conditions. Selecting the target normalized magnetizing current as zero assures BCM operation. The target for the normalized output voltage is selected as V_{TPn}, whose value will be calculated so the desired output RMS voltage equals to the reference voltage V_r. The expression of V_{TPn} will be derived in the next sections.

Replacing the target point $(i_{mn}, v_{on}) = (0, V_{TPn})$ in (24), the constant H in λ_{ON} is given by

$$H = \frac{\alpha}{\beta}\frac{V_{inn}}{i_{on}}V_{TPn}. \tag{25}$$

Therefore, the normalized BCM ON-state trajectory noted as σ_{ON} is given by

$$\sigma_{ON} := i_{mn} + \frac{\alpha}{\beta}\frac{v_{inn}}{i_{on}}v_{on} - \frac{\alpha}{\beta}\frac{v_{inn}}{i_{on}}V_{TPn} = 0. \tag{26}$$

Moving onto λ_{OFF}, A and B can be evaluated from the known target point as the initial conditions

$$i_{mn}\left(0^-\right) = 0,\ di_{mn}\left(0^-\right)/dt_n = -2\pi\alpha V_{TPn}. \tag{27}$$

Then, A and B can be expressed as

$$A = -i_{on},\ B = -V_{TPn}\sqrt{\alpha/\beta}. \tag{28}$$

Substituting (28) into (18), the complete normalized BCM OFF-state trajectory which is named as σ_{OFF} is defined as follows:

$$\sigma_{OFF} := \frac{\alpha}{\beta}v_{on}^2 + (i_{mn} - i_{on})^2 - \frac{\alpha}{\beta}V_{TPn}^2 - i_{on}^2 = 0. \tag{29}$$

E. BCM Control Law

This section explains the derivation of the control law based on the BCM trajectories from (26) and (29). The goal of the control law is to force the converter to move to and stay on the identified BCM trajectories. The control law is developed by knowing the movements along the trajectories for each state of transistor Q and the above conditions. Basically, the control law decides between two options: either Q should be turned ON

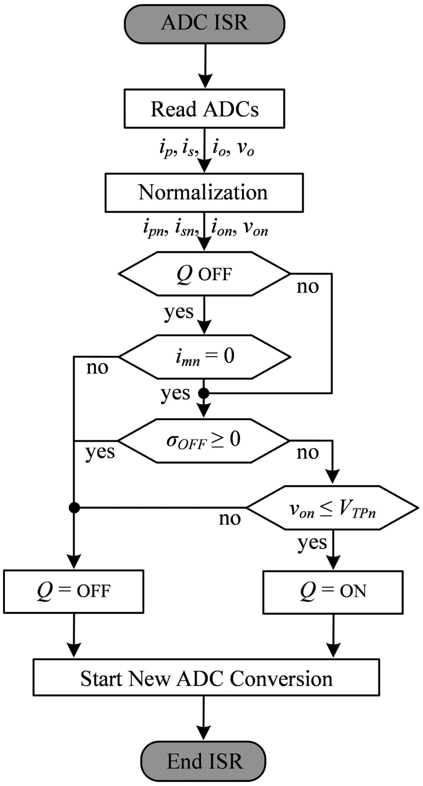

Fig. 6. Flow diagram of the BCM control law.

or OFF. The decision is based on the current state of transistor Q and the relative location of the current operating point with respect to the BCM trajectories.

While Q is ON, the converter moves up the i_{mn} versus v_{on} plane. If the converter is currently operating below σ_{OFF}, Q is kept ON if $v_{on} \leq V_{TPn}$, while the converter continues to move up the plane until σ_{OFF} is reached. Then, Q is turned OFF. If the converter were operating anywhere above σ_{OFF}, Q should be turned OFF.

Since the objective is to operate in BCM, Q is not allowed to switch back ON until $i_{mn} = 0$ p.u., once it has been switched OFF. Therefore, if the converter is operating anywhere above the v_{on} axis ($i_{mn} > 0$ p.u.) and Q is OFF, Q is kept OFF until the converter reaches the v_{on} axis. Once the v_{on} axis is reached, the current operating point is compared to σ_{OFF}. If the converter is operating at a point higher than σ_{OFF}, Q is kept OFF, allowing for the converter to evolve down the v_{on} axis to the OFF-state trajectory. After the converter is operating below or at σ_{OFF}, Q is switched ON if $v_{on} \leq V_{TPn}$, allowing for the converter to ride the ON-state trajectory back up to the OFF-state trajectory as previously described.

Fig. 6 shows a complete flow diagram of the BCM control law [33], which forces the converter to move and operate under the BCM trajectories in one switching cycle, no matter where the converter is currently operating. This allows the flyback converter to operate in BCM continuously for any load during steady-state conditions. Under transient conditions where the input voltage or load changes when Q is OFF, the worst-case scenario would be that the converter recovers in two switching cycles. During that transient, a DCM operation with a slightly overvoltage at the output or BCM operation with a slightly undervoltage at the output could be experienced. This is because the desired ON- and OFF-state trajectories change when the converter parameters change. If the disturbance occurs while Q is ON, the converter will reach the target point in only a single switching cycle. The rapid recovery time of one switching cycle provides remarkable stability and transient response time for all converter conditions.

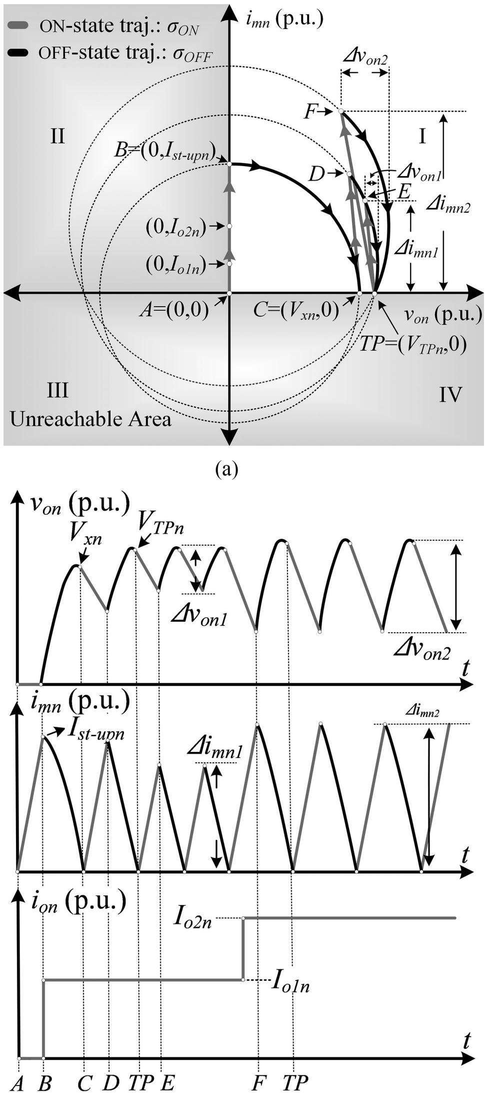

(a)

(b)

Fig. 7. (a) NSS trajectories for the flyback converter operating in BCM when $\alpha/\beta = 1$. (b) Normalized output voltage v_{on}, magnetizing inductance current i_{mn}, and output current i_{on}.

III. START-UP AND STEADY-STATE CHARACTERISTICS

The normalized trajectories and main waveforms for a flyback converter operating in BCM when $\alpha/\beta = 1$ are shown in Fig. 7 [33]. At the converter startup, initially i_{mn}, v_{on}, and i_{on} are zero (see point A in Fig. 7). When Q turns ON, i_{mn} starts increasing, while v_{on} stays at zero. When σ_{ON} intersects σ_{OFF} at point $B = (0$

p.u., $I_{\textit{st-upn}}$), Q turns OFF so i_{mn} decreases while v_{on} increases. As soon as v_{on} starts rising, i_{on} moves toward its rated level I_{o1n} if the load is connected. Therefore, the first intersection of σ_{OFF} with the v_{on} axis will be at V_{xn}, whose level is lower than the target point V_{TPn} because σ_{OFF} was calculated for $i_{on} = 0$ p.u.. When $i_{mn} = 0\,$p.u., Q turns ON at point $C = (V_{xn},\, 0\,\text{p.u.})$ until σ_{OFF} is reached at point D where Q turns OFF. The next intersection with the v_{on} axis is at the target point $TP = (V_{TPn},\, 0\,\text{p.u.})$ where steady-state conditions are reached and the flyback operates between points *E* and *TP*. In case of a sudden load change while Q is ON, the controller will be able to reach steady-state conditions in only one switching cycle. In that case, the converter will be operating from points *F* to *TP*. The expressions for the start-up and steady-state conditions of Fig. 7 are calculated, and their dependence to the converter parameter uncertainties is analyzed in the following sections.

A. Start-Up Peak Current

The normalized start-up peak current $I_{\textit{st-upn}}$ with start-up initial conditions $(i_{on},\, v_{on}) = (0,\, 0)$ p.u. can be determined by evaluating σ_{OFF} (29) yielding

$$I_{\textit{st-upn}} = \sqrt{\alpha/\beta}\, V_{TPn}. \tag{30}$$

Fig. 8(a) shows $I_{\textit{st-upn}}$ as function of α/β when $V_{TPn} = 1\,$p.u. $I_{\textit{st-upn}} = 1\,$p.u. that only happens under ideal conditions ($\alpha/\beta = 1$). De-normalizing (30) by using (8) and (11), the start-up peak current $I_{\textit{st-up}}$ can be calculated as follows:

$$I_{\textit{st-up}} = \sqrt{\frac{\alpha}{\beta}\frac{\bar{C}_o}{\bar{L}_m}}\, V_{TP}. \tag{31}$$

$I_{\textit{st-up}}$ is proportional to the square root of $\bar{C}_o/\bar{L}_m$ and V_{TP}; so $I_{\textit{st-up}}$ could be very high for high-voltage and low-ripple applications. This is because, $I_{\textit{st-up}}$ is the necessary magnetizing current to reach the target point in a single switching action when $i_{on} = 0$ p.u. If necessary, the start-up current can be limited to a lower value I_{max} at the expense of reaching the target point under start-up conditions in more than a single switching action. Normally under start-up conditions, $\alpha/\beta = 1$ since the flyback converter is supposed to have the parameters used in the design process.

B. Start-Up Output Voltage

If the load is connected during startup, the first intersection with the v_{on} axis will not be at the target point V_{TPn}. Instead, it will be at a lower point defined as the start-up output voltage V_{xn}. Also, V_{xn} will be lower than V_{TPn} if the start-up current is limited to I_{maxn}, even if the load is disconnected. Modifying the initial conditions of (18), the normalized start-up output voltage V_{xn} can be derived as follows:

$$V_{xn} = \sqrt{\frac{I_{maxn}\,(I_{maxn} - 2i_{on})}{\alpha/\beta}}. \tag{32}$$

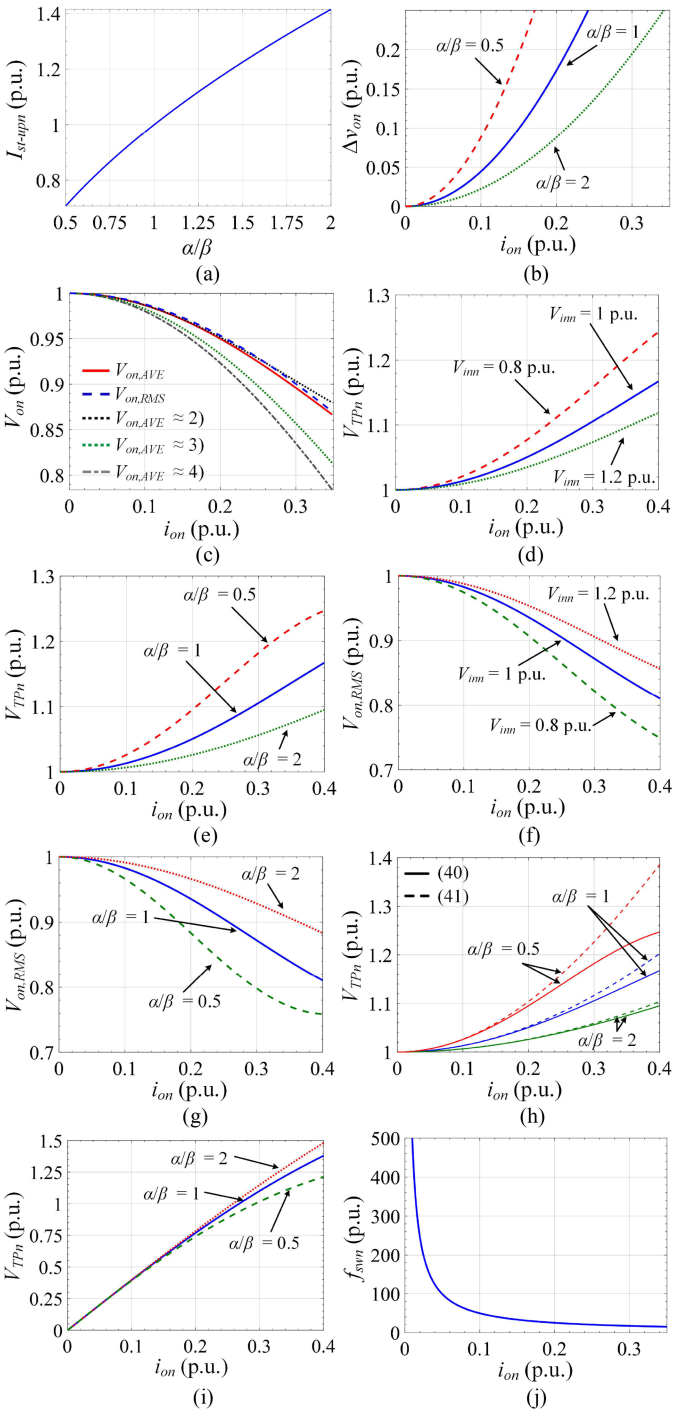

Fig. 8. (a) Normalized start-up current $I_{\textit{st-upn}}$ to reach the target point $V_{TPn} = 1\,$p.u. with minimum number of switching actions. (b) Normalized output voltage ripple Δv_{on} with $v_{inn} = 1\,$p.u. (c) RMS, average, and approximations for the output voltage v_{on}. (d) Normalized output voltage target point V_{TPn} to obtain $V_{on,RMS} = 1$ p.u. with $\alpha/\beta = 1$ and v_{inn} changing. (e) Normalized output voltage target point V_{TPn} to obtain $V_{on,RMS} = 1$ p.u. with $v_{inn} = 1\,$p.u. and α/β changing. (f) Normalized RMS output voltage when $V_{TPn} = 1\,$p.u. with $\alpha/\beta = 1$ and v_{inn} changing. (g) Normalized RMS output voltage when $V_{TPn} = 1\,$p.u. with $v_{inn} = 1$ and α/β changing. (h) Normalized output voltage target point plotted from (40) and its low-ripple approximation from (41). (i) Normalized magnetizing current ripple ΔI_{mn} with $v_{inn} = 1\,$p.u. and α/β changing. (j) Normalized switching frequency f_{swn} as function of the load current i_{on}.

The use and importance of V_{xn} on the design of the proposed adaptive boundary controller will be addressed in the following section. By de-normalizing (32), the start-up voltage V_x is given by

$$V_x = \sqrt{I_{max}\frac{\bar{L}_m}{\bar{C}_o}\frac{\beta}{\alpha}\left(I_{max} - \frac{2i_o}{n}\right)}. \tag{33}$$

C. Output Voltage Ripple

Under steady-state conditions, the voltage ripple Δv_{on} is defined by the difference between the maximum and minimum points of the voltage waveform. An expression for v_{on} as a function of i_{mn} can be obtained from σ_{OFF} as follows:

$$v_{on} = \sqrt{V_{TPn}^2 + 2\frac{\beta}{\alpha}i_{mn}i_{on} - \frac{\beta}{\alpha}i_{mn}^2}. \tag{34}$$

Since the locus of σ_{OFF} is an ellipse whose principal axes are aligned with the i_{mn}, v_{on} axes, the normalized maximum output voltage $V_{on,max}$ is obtained for $i_{mn} = i_{on}$ as

$$V_{on,max} = \sqrt{V_{TPn}^2 + \frac{\beta}{\alpha}i_{on}^2}. \tag{35}$$

De-normalizing (35), the maximum output voltage $V_{o,max}$ can be then expressed as

$$V_{o,max} = \sqrt{V_{TP}^2 + \frac{\bar{L}_m}{\bar{C}_o}\frac{\beta}{\alpha}\frac{i_o^2}{n^2}}. \tag{36}$$

The minimum value for the normalized output voltage $V_{on,min}$ is obtained from the intersection of σ_{OFF} with σ_{ON} as

$$V_{on,min} = \frac{V_{TPn}v_{inn}^2\frac{\alpha}{\beta} - i_{on}^2\left(V_{TPn} + 2v_{inn}\right)}{i_{on}^2 + v_{inn}^2\frac{\alpha}{\beta}}. \tag{37}$$

Then, the normalized output voltage ripple is calculated as

$$\Delta v_{on} = \sqrt{V_{TPn}^2 + i_{on}^2\frac{\beta}{\alpha}} + \frac{i_{on}^2\left(V_{TPn} + 2v_{inn}\right) - V_{TPn}\frac{\alpha}{\beta}v_{inn}^2}{i_{on}^2 + \frac{\alpha}{\beta}v_{inn}^2}. \tag{38}$$

Fig. 8(b) illustrates (38) as function of i_{on} for different values of α/β when $v_{inn} = 1$ p.u.. For low-output voltage ripple applications ($\Delta v_o < 5\%$ of V_r), i_{on} should not exceed 0.1 p.u. under ideal conditions. If $\alpha/\beta > 1$, Δv_{on} will decrease since the actual values of C_o will be greater than that used in the design process.

D. Normalized Output Voltage Target Point

The target point of the output voltage V_{TPn} should be selected so that the normalized average output voltage $V_{on,AVE} = 1$ p.u.. $V_{on,AVE}$ should be obtained by integrating v_{on} over a normalized switching period T_{swn}; but the exact evaluation of $V_{on,ave}$ is cumbersome. However, the integral complexity is reduced if the RMS of v_{on} is calculated instead of the average value, and also, it is possible to obtain an approximated expression which is useful for low-ripple cases. Furthermore, the RMS and the average values will be similar since Δv_{on} is small in comparison with the output voltage.

Considering the complexity of the exact evaluation of $V_{on,AVE}$, different simplified calculations can be made to obtain an approximated expression for $V_{on,AVE}$.

Among them:

1) Evaluating $V_{on,RMS}$ instead of $V_{on,AVE}$
2) $V_{on,AVE} \approx \delta(V_{on,min} + V_{TPn})/2 + (1-\delta)(V_{on,max} + V_{TPn})/2$, where δ is the fraction of time where v_{on} is lower than V_{TPn};
3) $V_{on,AVE} \approx (V_{on,max} + V_{on,min})/2$;
4) $V_{on,AVE} \approx (V_{TPn} + V_{on,min})/2$.

In all cases, $V_{on,max}$ is the output voltage corresponding to the time in which i_{mn} matches i_{on} reflected back to the primary side, and $V_{on,min}$ is the voltage value obtained at the time when Q is turned OFF.

Those alternative expressions are compared with a numerical evaluation of $V_{on,AVE}$ in Fig. 8(c) for a specific design and fixed target operation point $V_{TPn} = 1$, and it is seen that the alternatives 1) and 2) are better approximations to $V_{on,AVE}$ than 3) and 4).

Based on these results, $V_{on,RMS}$ can be considered as a good approximation for $V_{on,AVE}$ and it is shown below that it can be calculated in closed form rather easily.

Although expression 2) seems to be accurate enough and easier than $V_{on,RMS}$, when $V_{on,min}$ and $V_{on,max}$ are included as functions of the other variables and parameters, the complexity increases. Also, parameter δ needs to be defined on an empirical basis.

Therefore, the RMS $V_{o,RMS}$ is calculated as follows:

$$V_{o,RMS} = \sqrt{\frac{1}{T_{swn}}\int_0^{T_{swn}}\left(v_{on}(t_n)\right)^2 dt_n} = \sqrt{\frac{1}{T_{swn}}\left(I_1 + I_2\right)} \tag{39}$$

where

$$I_1 = \int_0^{I_{mn,max}}\left(V_{TPn} - \frac{\beta}{\alpha}\frac{i_{on}}{v_{inn}}i_{mn}\right)^2\frac{di_{mn}}{2\pi\alpha v_{inn}}$$

and

$$I_2 = \int_{I_{mn,max}}^0\left(\sqrt{V_{TPn}^2 + 2i_{mn}i_{on}\frac{\beta}{\alpha} - i_{mn}^2\frac{\beta}{\alpha}}\right)^2\frac{di_{mn}}{-2\pi\alpha V_r}.$$

$V_{on,RMS} = 1$ p.u. is replaced in (39) since the desired output voltage is equal to the reference level V_r. Solving for V_{TPn}, the expression is obtained (40) shown at the bottom of this page.

Fig. 8(d) shows V_{TPn} as function of i_{on} when $\alpha/\beta = 1$ and 0.8 p.u. $< v_{inn} <$ 1.2 p.u., and Fig. 8(e) displays V_{TPn} as

$$V_{TPn} = \frac{\left(\frac{\alpha}{\beta}v_{inn}^2 + i_{on}^2\right)\left(v_{inn} + 1\right)\left(3v_{inn}^3\frac{\alpha}{\beta} + \sqrt{3v_{inn}^3\frac{\alpha}{\beta}\left(3v_{inn}\frac{\alpha}{\beta} - 2v_{inn}i_{on}^2 + 2i_{on}^2\right) + 3i_{on}^4(-3v_{inn}^2 + 2v_{inn} + 1)}\right)}{i_{on}^4(3v_{inn} + 1) + 3v_{inn}^4\left(\frac{\alpha}{\beta}\right)^2 + 3v_{inn}^5\left(\frac{\alpha}{\beta}\right)^2 + 2v_{inn}^3\frac{\alpha}{\beta}i_{on}^2} - v_{inn} \tag{40}$$

function of i_{on} when $v_{inn} = 1$ p.u. and $0.5 < \alpha/\beta < 2$. If $i_{on} < 0.1$ p.u., V_{TPn} should only change about 1% to keep the RMS output voltage at the rated level. Therefore, while keeping $V_{TPn} = 1$, $V_{on,RMS}$ will decrease by about 1.5% when $i_{on} < 0.1$ p.u., and less than 0.05% when $i_{on} < 0.05$ p.u. as seen in Fig. 8(f) and (g). Therefore, V_{TPn} could remain at 1 for a design where $\Delta v_{on} < 5\%$ and $i_{on} < 0.1$ p.u. without having a large output error. Otherwise, the target point can be evaluated as a function of the load condition using (40) or using the following simplified approximation valid for low-ripple cases which were obtained by first assuming $v_{inn} \approx 1$ which simplifies the square root term on (40), and then considering zero the terms i_{on}^4

$$V_{TPn} = \left(3\frac{\alpha}{\beta} + 5i_{on}^2\right) \Big/ \left(3\frac{\alpha}{\beta} + i_{on}^2\right). \tag{41}$$

Fig. 8(h) shows V_{TPn} as function of i_{on} using (40) and compared to (41) for different values of α/β illustrating that the approximation works very well under low-ripple conditions.

E. Normalized Magnetizing Inductance Current Ripple

The current ripple through the magnetizing inductance Δi_{mn} is equal to the peak current $I_{mn,max}$ which can be calculated by replacing $V_{on,min}$ on the BCM trajectory σ_{ON} and then solving for the magnetizing current yielding

$$I_{mn,max} = \Delta i_{mn} = 2\frac{\alpha}{\beta} i_{on} v_{inn} (V_{TPn} + v_{inn}) \Big/ \left(i_{on}^2 + \frac{\alpha}{\beta} v_{inn}^2\right). \tag{42}$$

Fig. 8(i) shows the plot of (42) when $v_{inn} = 1$ p.u. and α/β changes. De-normalizing (42), the maximum magnetizing inductance current $I_{m,max}$ for a given operating steady-state condition can be calculated by

$$I_{m,max} = 2\frac{\alpha}{\beta} i_o v_{in} \left(V_r + \frac{v_{in}}{n}\right) \Big/ \left(i_o^2 \frac{\bar{L}_m}{\bar{C}_o} + \frac{\alpha}{\beta} v_{in}^2\right). \tag{43}$$

F. Switching Frequency

The converter switching frequency f_{sw} will change based on the load, input voltage, and parameter variations because of the operation in BCM. The derivation of f_{sw} is done by calculating the normalized switching period T_{swn} from the ON- and OFF-time periods obtained from (15) and (21); in particular

$$T_{swn} = T_{ONn} + T_{OFFn} = \frac{\Delta i_{mn}}{2\pi\alpha} \left(\frac{1}{v_{inn}} + \frac{1}{v_{on}}\right). \tag{44}$$

By de-normalizing (44), f_{sw} is obtained as

$$f_{sw} = f_{swn} f_r = (\alpha v_{in} V_r) \big/ \left(\bar{L}_m \Delta i_m \left(V_r + v_{in}/n\right)\right). \tag{45}$$

Fig. 8(j) displays the normalized switching frequency f_{swn} as a function of the load current. The switching frequency for BCM operation increases when the load current decreases. Due to the converter topology, the averaged diode current must be equal to the averaged load current for a constant averaged output voltage. Therefore, the same must happen with the averaged diode current, which depends linearly on the peak magnetizing current, if the load current decreases. During the whole OFF-interval, the diode current decreases at an approximately constant rate which depends on the output voltage, and the switching frequency increases inversely proportional to the peak of the magnetizing current.

As the maximum switching frequency is limited by the used hardware, BCM operation cannot be sustained for load currents falling below a certain limit. For lower load currents, DCM operation is necessary.

IV. ADAPTIVE BCM CONTROL LAW

As analyzed in the previous section, the transient and steady-state responses of the converter under NSS control may not be as good as theoretically expected when the actual parameters of the flyback L_m and C_o are not equal to the nominal values $\bar{L}_m$ and $\bar{C}_o$ used in the design. This occurs because the derived BCM control trajectories are obtained by normalizing the differential equations of the converter with base values that may differ from the actual ones. This section presents a novel BCM NSS control method that compensates for the parametric uncertainties of the converter. The proposed controller (29) responds by adapting the ratio α/β whenever it detects that the system is not evolving on the ideal trajectories. The adaptation is performed at the end of each switching cycle using the following rule which produces small adjustments on α/β proportional to the difference between the normalized target points V_{TPn} and V_{xn}

$$\alpha/\beta\,(n+1) = \alpha/\beta\,(n) + \left(V_{TPn} - V_{xn}\,(n)\right) K \tag{46}$$

where the constant K is a real number selected by the designer, and $\alpha/\beta(n)$ and $V_{xn}(n)$ are the actual values of the parameter ratio and measured target point voltage to obtain the future value $\alpha/\beta(n+1)$. A brief description and justification of the adaptation algorithm is presented below.

The proposed BCM trajectories (26) and (29) model the converter uncertainties with the introduction of the parameter α/β, so an ideal control performance could be always obtained if α/β is precisely estimated. The first estimation of α/β is performed during the startup and then small adjustments will be implemented based on the measured error to the desired target point after each switching cycle. The complete control scheme is shown in Fig. 9 and explained in the following. After each analog-to-digital conversion, the normalization is performed using (8) through (12). The measured variables are the transformer primary- and secondary-side currents i_p and i_s, output current i_o, and output voltage v_o. The magnetizing current i_m is obtained from i_p and i_s. When Q is ON, i_{mn} equals the normalized transformer primary-side current i_{pn}, and when Q is OFF, i_{mn} is the secondary side one i_{sn}. The reference voltage V_r, the reference impedance Z_r, the maximum start-up current I_{max}, and the voltage target point V_{TP} ($V_{TP} \approx V_r$ for low-ripple applications as presented in Section III-D) are the only constants required for the controller. At the beginning (see point *A* in Fig. 7), i_{mn}, i_{on}, and v_{on} are zero, α/β is 1, producing a negative value in the calculation of σ_{OFF}. Those are the initial conditions of the converter. The transistor remains ON until either σ_{OFF} is intersected ($\sigma_{OFF} \geq 0$) or the start-up current limit is reached ($i_{mn} \geq I_{maxn}$). *Startup* is a variable used to determine if the converter is under

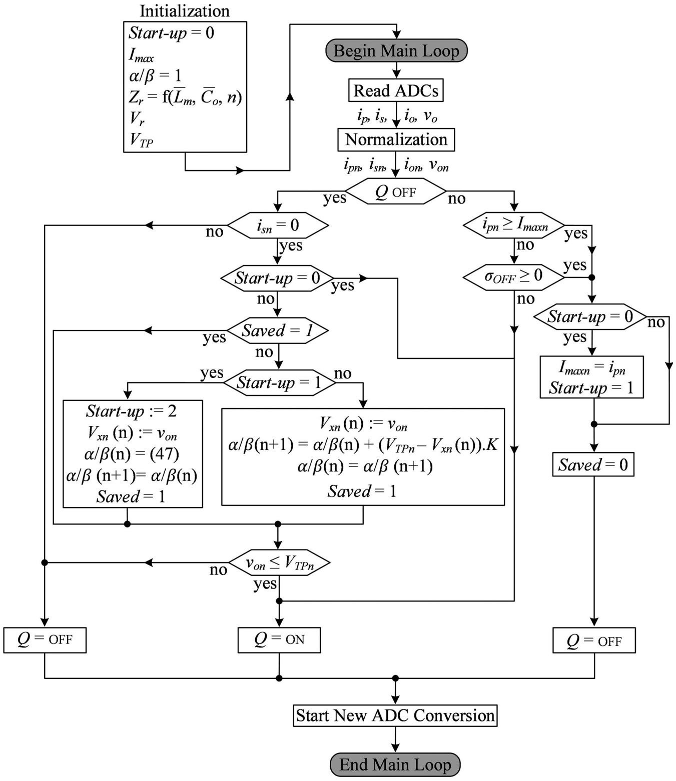

Fig. 9. Flow diagram of the adaptive BCM NSS control law.

start-up or steady-state conditions; initially, *Startup* $= 0$ until Q turns OFF the first time.

Just before turning Q OFF for the first time (see point B in Fig. 7), the normalized start-up current $I_{st\text{-}upn}$ is saved in the variable I_{maxn} and the variable *startup* is set to 1. Later, I_{maxn} will be used for the initial estimation of α/β. Transistor Q will be kept OFF until the v_{on} axis is reached and $v_{on} \leq V_{TPn}$ (see point C in Fig. 7). As soon as the v_{on} axis is intersected, v_{on} will be saved into the variable V_{xn} and startup is set equal 2. Then, the first estimation for α/β is derived using (32)

$$\alpha/\beta = I_{maxn}\left(I_{maxn} - 2i_{on}\right)/V_{xn}^2. \tag{47}$$

The next time σ_{OFF} is calculated, it will be using the just updated α/β obtained from (47). Then, Q will turn ON again after v_{on} is less than the target point V_{TPn}. Therefore, the flyback in case of an overvoltage will operate in DCM during that transient. The overvoltage is related to cases where the true value of α/β is lower than the current estimation [see Fig. 8(d)]; otherwise, Q will turn ON right after i_{mn} reaches zero and the new α/β is calculated.

Similarly to start-up conditions, Q will stay ON until $i_{mn} \geq I_{max}$ or $\sigma_{OFF} \geq 0$ but now it is not necessary to save anymore the peak value of the magnetizing current for the α/β calculation. After Q turns OFF and when i_{mn} reaches zero p.u., v_{on} is saved into V_{xn}.

The convergence and performance of the adaptation rule (46) are analyzed next. By differentiating (41) with respect to α/β, the following is obtained:

$$dV_{TPn}/d\left(\alpha/\beta\right) = -12i_{on}^2/\left(3\alpha/\beta + i_{on}^2\right)^2 = -G\left(n\right) < 0. \tag{48}$$

As this kind of converters do not operate adequately when the output current is zero because the output capacitor which holds the output voltage cannot be discharged, it is reasonable to consider that the output current is always greater than a minimum operating value $I_{on,min}$. So, it will always be $G(n) \geq G_{min}$, where G_{min} is obtained evaluating (48) at $I_{on,min}$. Also, a maximum value G_{max} can be evaluated from (48) by considering the maximum possible value of the output current $I_{on,max}$, and the minimum possible value for α/β. Since $I_{on,max}$ should be at most equal to 1 and α/β will never reach zero because it would imply to consider a null nominal magnetizing inductance in the design, it can be shown that for $\alpha/\beta > 0.1$, G will never be greater than 10, and usually will be lower than 4 considering a 50% error in the nominal parameters.

Approximating (48) as function of the actual and future values of V_{xn} and α/β yields

$$\frac{V_{xn}\left(n+1\right) - V_{xn}\left(n\right)}{\alpha/\beta\left(n+1\right) - \alpha/\beta\left(n\right)} = -G\left(n\right). \tag{49}$$

By solving $\alpha/\beta(n+1) - \alpha/\beta(n)$ from (46), replacing it into (49), and rearranging the actual and future terms, the following expression is obtained:

$$V_{xn}\left(n+1\right) - V_{xn}\left(n\right)\left(1 + KG\left(n\right)\right) + V_{TPn}KG\left(n\right) = 0. \tag{50}$$

By applying the Z-transform to (50), assuming that the gain G is constant and the input V_{TPn} is a step signal, and solving for $V_{xn}(z)$, the stability of the target point can be analyzed

$$V_{xn}\left(z\right) = -\frac{V_{TPn}KG}{z - \left(1 + KG\right)}. \tag{51}$$

By analyzing the poles of (51), the target point is exponentially stable without oscillatory behavior if and only if $0 < 1 + K.G < 1$ or, equivalently, $-1/G < K < 0$. So, considering the worst case, the gain K should be

$$-1/G_{max} < K < 0 \tag{52}$$

to assure exponential stability, and, therefore, V_{xn} will converge toward V_{TPn} which also implies from (46) that α/β will converge to a constant final value. That can be also noted from the final value theorem applied to (51) and considering that V_{TPn} is a step signal

$$\lim_{z\to 1}\left(-\left(z-1\right)V_{TPn}\frac{z}{z-1}\frac{KG}{z-1-KG}\right) = V_{TPn}. \tag{53}$$

When considering $G = G_{min}$ in (50), the dynamic response will be the slowest one and will provide an upper bound for any other dynamics obtained with other gains G such that $G_{max} > G > G_{min}$ for the same initial conditions and input signal. Therefore, any dynamic response obtained from (50) for K satisfying (52) and considering a variable $G(n)$, such that $G_{max} > G(n) > G_{min}$, will also be exponentially asymptotically stable.

TABLE II
FLYBACK CONVERTER PARAMETERS

Parameter	Value
v_o	24 V
i_o	0.5 A
v_{IN}	6 V
Δv_o	4V
Δi_m	10 A
f_{sw}	7 kHz

V. DESIGN PROCEDURE AND EXAMPLE

The specifications for the proposed BCM flyback converter are presented in Table II. The output voltage and magnetizing current ripples in the proposed design example will be exaggerated in order to improve the visualization and facilitate the plot of the trajectories. In addition, a low ripple case will be illustrated. The step-by-step design process is given next assuming that $\alpha/\beta = 1$.

A. Transformer Turns Ratio

The turns ratio *n* is calculated by dividing the transformer rated primary and secondary voltages. The latest produces a duty cycle about 50% at rated conditions since $v_{inn} \approx V_{on,AVE}$ [see T_{ONn} and T_{OFFn} from (44)]. Then

$$n = N_p/N_s = v_{in}/v_o = 1/4. \tag{54}$$

B. Output Capacitance

The frequency f_{sw} depends on the load conditions in BCM operation. However, a desired f_{sw} can be selected for rated conditions. By de-normalizing and solving (23) for Δi_{mn}, the following expression for Δi_m is obtained:

$$\Delta i_m = \frac{v_{in}\Delta v_o \bar{C}_o}{i_o \bar{L}_m}. \tag{55}$$

By substituting (55) into (45) and solving for $\bar{C}_o$, the output capacitance needed to operate with a voltage ripple Δv_o and a switching frequency f_{sw} when the output current is i_o is obtained as follows:

$$\bar{C}_o = \frac{i_o}{2f_{sw}\Delta v_o} \approx 10\ \mu\text{F}. \tag{56}$$

C. Magnetizing Inductance

By de-normalizing (23) and solving for $\bar{L}_m$, the following expression based on the design specifications is derived:

$$\bar{L}_m = \left(v_{in}\Delta v_o \bar{C}_o\right)/(i_o \Delta i_m) \approx 45\,\mu\text{H}. \tag{57}$$

There is a tradeoff between Δi_{mn} and L_m since a lower Δi_{mn} implies a higher at the expense of increasing the transformer cost. However, a higher Δi_{mn} increases the rating of the semiconductor devices.

D. Reference Impedance

The reference impedance Z_o is obtained from the previously calculated parameters by using (54), (56), and (57)

$$Z_o = (1/n)\sqrt{\bar{L}_m/\bar{C}_o} = 8.35\ \Omega. \tag{58}$$

E. Start-Up Current

$I_{st\text{-}up}$ is obtained by substituting the calculated $\bar{C}_o$ and $\bar{L}_m$ parameters into (31)

$$I_{st\text{-}up} = V_r\sqrt{\bar{C}_o/\bar{L}_m} \approx 11.3\ \text{A}. \tag{59}$$

F. Steady-State Peak Magnetizing Current

The peak current during rated steady-state conditions $I_{m,max}$ is obtained from (43) as follows:

$$I_{m,max} = (4i_o v_{in} V_r)\,/\left(i_o^2 \bar{L}_m/\bar{C}_o + v_{in}^2\right) \approx 7.75\ \text{A}. \tag{60}$$

G. Transistor Current and Voltage Ratings

The transistor current rating $I_{Q,max}$ must be higher than $I_{st\text{-}up}$ if the start-up current is not limited. If it is desired to limit the transistor current to a lower value I_{max}, it should be greater than the steady-state value, that is,

$$I_{st\text{-}up} > I_{max} > I_{m,max}. \tag{61}$$

The transistor voltage rating $V_{Q,max}$, without considering the voltage spikes related to transformer leakage inductance is given by

$$V_{Q,max} > v_{in} + v_o n. \tag{62}$$

Therefore, in practice, $V_{Q,max}$ will depend on the type of the snubber circuit used and the transformer leakage inductance [35].

H. Diode Current and Voltage Ratings

The current and voltage ratings of the diode *d* can be obtained from (61) and (62) referred to the secondary side. Then, the breakdown voltage of the diode $V_{d,max}$ should be higher than

$$V_{d,max} > v_{in}/n + v_o. \tag{63}$$

In case that $I_{st\text{-}up}$ is limited to $I_{m,max}$, the diode current rating should be

$$I_{st\text{-}up} n > I_{d,max} > I_{m,max} n. \tag{64}$$

VI. SIMULATION RESULTS

MATLAB/Simulink simulations for a flyback with electrical parameters from Table II and nominal components from Table III are presented under different α/β conditions starting with the BCM NSS control scheme in Fig. 6. Initially, ideal conditions ($\alpha/\beta = 1$) are considered. During the startup, v_o and i_o are zero, so the expected start-up voltage V_x and current $I_{st\text{-}up}$

TABLE III
EXPERIMENTAL PROTOTYPE CHARACTERISTICS

Parameter	Value
Transformer T	Coilcraft® NA5919-AL, L_m = 45.8 µH, n = 1/4, I_{sat} = 13.6 A @ L_m = 38.5 µH
Transistor Q	Vishay® IRFP140PBF V_{dss} = 100 V, I_D = 31 A @ 25 °C
Diode D	Vishay® VS-8TQ100PBF V_R = 100 V, I_D = 8 A, V_F = 0.58 V
Output Capacitor C_o	10.52 µF Film

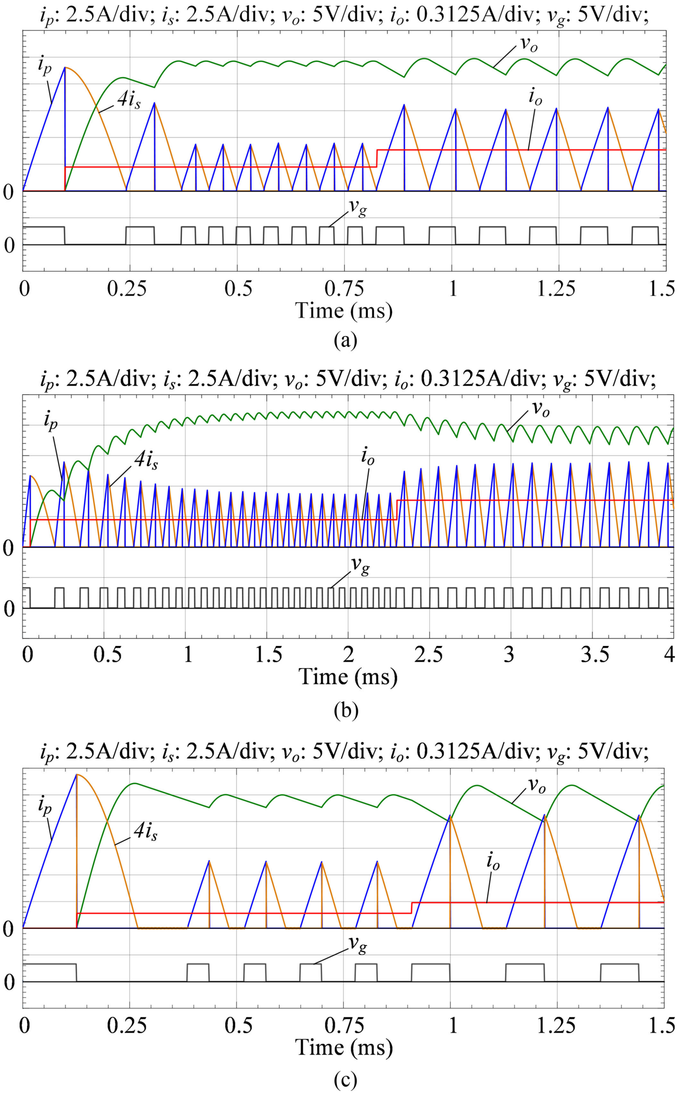

Fig. 10. Simulation results of BCM NSS control law. (a) Under ideal conditions. (b) When $\alpha/\beta = 4$. (c) When $\alpha/\beta = 0.64$.

are calculated from (33) and (31) as

$$V_x = \sqrt{I_{max}\frac{\bar{L}_m}{\bar{C}_o}\frac{\beta}{\alpha}\left(I_{max}-\frac{2.i_o}{n}\right)} - V_d = 20.95\ \text{V}$$

$$I_{st\text{-}up} = V_{TP}\sqrt{\bar{C}_o/\bar{L}_m} = 11.5\ \text{A}.$$

From the simulation results shown in Fig. 10(a), $I_{st\text{-}up} = 11.54$ A and $V_x = 21.08$ V, representing errors of 0.35% and 0.62%, respectively. Thus, there is good agreement between simulation and theoretical results. Moreover, the controller is able to react to an output current step change from 0.28 to 0.48 A in only one switching cycle.

Next, a flyback with parameter uncertainties $\alpha/\beta = 4$, which could be the case where $\bar{C}_o = C_o/4$ and $\bar{L}_m = L_m$, is simulated. From (31) and (33), the expected start-up parameters should be $I_{st\text{-}up} = 5.75$ A and $V_x = 8.79$ V. Simulation results are presented in Fig. 10(b) where $I_{st\text{-}up} = 5.85$ A and $V_x = 9.06$ V, representing errors of 1.7% and 3.07%, respectively. In this case, the errors are caused by the quantization of the signals, as decreasing the sampling time reduces the error. Moreover, the controller due to the parameter uncertainties will not reach the target voltage and has poor voltage regulation as the output current changes.

Next, a case where $\alpha/\beta = 0.64$ is considered. That case could occur if, for example, $\bar{C}_o = C_o/0.64$ and $\bar{L}_m = L_m$. The calculated start-up parameters are $I_{st\text{-}up} = 14.38$ A and $V_x = 26.99$ V, while the parameters from the simulation results in Fig. 10(c) are 14.41 A and 27.04 V, which represent errors of 0.21% and 0.18%, respectively. In this case, the controller due to the parameter uncertainties is operating in DCM instead of BCM. When the load increases, the time where the diode current is zero also increases.

Then, the novel adaptive BCM NSS controller was simulated to show its effectiveness against parameter uncertainties. First, the adaptive controller is simulated for the case when $\alpha/\beta = 4$, and the results are shown in Fig. 11(a). In this case, the controller estimated $\alpha/\beta = 3.982$, which represents an error of 0.45%. Due to this estimation, the controller is able to track properly the reference voltage and is able to react to disturbance in the output current in one switching cycle.

Finally, the adaptive controller was simulated for the case when $\alpha/\beta = 0.64$, and the simulation results are illustrated in Fig. 11(b). In this case, the controller estimated $\alpha/\beta = 0.6401$, which represents an error of 0.016%. Due to this estimation, the controller is able to operate in BCM instead of DCM.

VII. EXPERIMENTAL VERIFICATION

A flyback converter with the specifications of Table II and the components of Table III was built and tested. The output capacitor C_o was specifically designed in this first experiment with academic purposes to lead to a large output voltage ripple, so the figures can show clearly the behavior of the system. Later in this section, other results are included after replacing this capacitor by a larger one leading to a lower output voltage ripple to show a more realistic and practical application. The traditional and novel adaptive BCM NSS control laws were implemented using the TMS320F28335 DSP from Texas Instruments. First, the BCM NSS control law was verified under ideal conditions and with parameter variations. Then, the adaptive control law was executed under similar conditions as those in the previous tests and a detailed comparison was performed. Fig. 12(a) presents

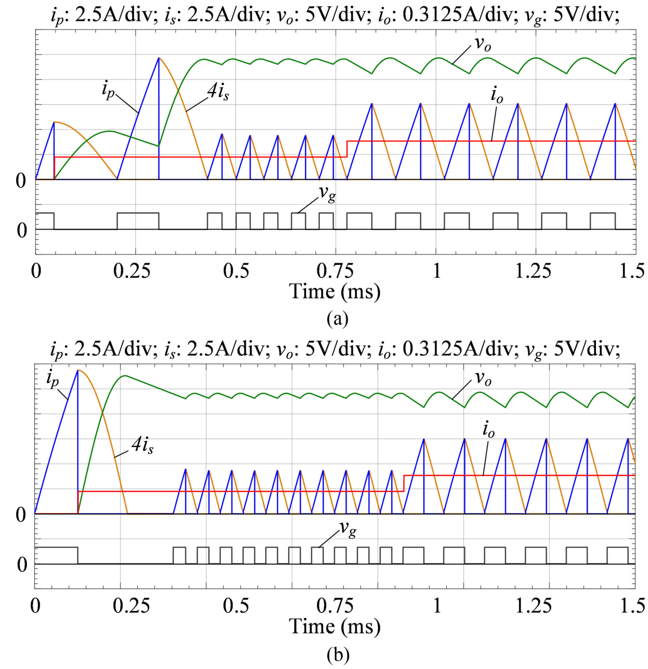

(a)

(b)

Fig. 11. Simulation results of the adaptive BCM NSS control law when (a) $\alpha/\beta = 4$ and (b) $\alpha/\beta = 0.64$.

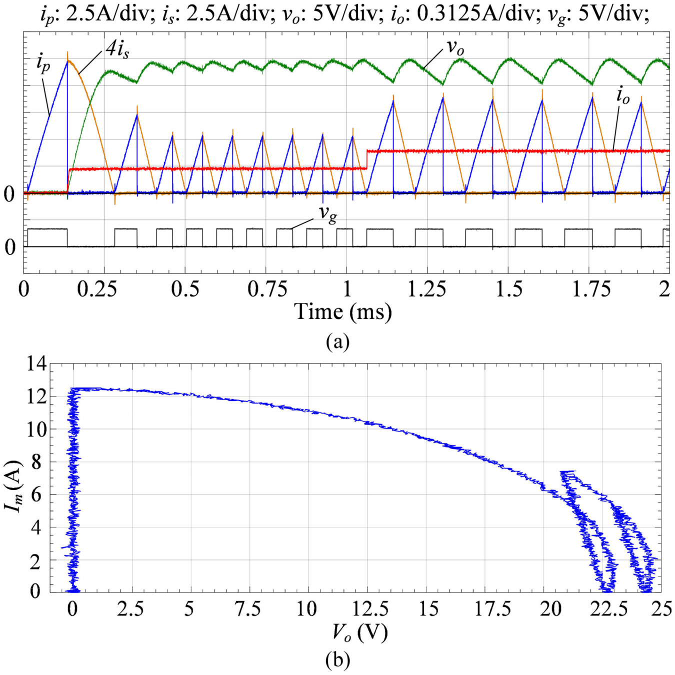

(a)

(b)

Fig. 12. (a) Transient response and (b) state-plane trajectory for the BCM NSS control law under ideal conditions.

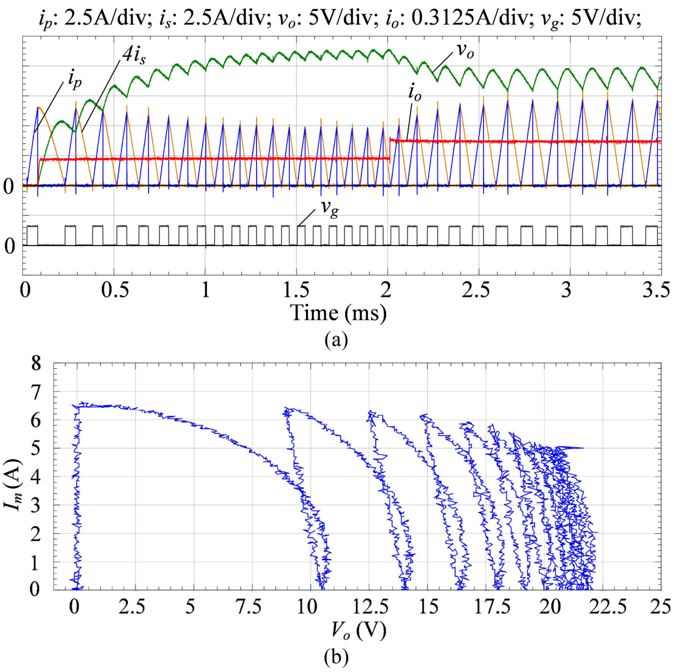

(a)

(b)

Fig. 13. (a) Transient response and (b) state-plane trajectory for the BCM NSS control law when $\alpha/\beta = 4$.

the transient response of the BCM NSS control law shown in Fig. 6 under ideal conditions. The primary and secondary transformer currents i_p and i_s; the output voltage and current i_o and v_o, as well as the DSP gate signal v_g are shown in the same figure. At start-up i_o and v_o are zero, Q turns ON until σ_{OFF} is reached when $I_{st\text{-}up}$ is 12.25 A which is slightly higher than the 11.52 A value calculated by replacing on (31) the converter parameters of Table III. This is due to the processing time delay introduced by the DSP while computing the control structure. Once Q is OFF, i_o increases to its steady-state value (∼0.28 A) and the voltage V_x when i_s reaches zero is 22.68 V while the calculated value using (33) is 22.95 V. These demonstrate the accuracy of the derived trajectories and equations. During the next switching cycle, v_o will reach to the target point $V_{TP} = 24$ V and steady-state conditions as appreciated in Fig. 12(a). At the tenth switching cycle, there is a sudden load increase of about 100% of its initial value. The controller was able to reach the target point in only a switching cycle since the load disturbance occurred while Q was ON, so σ_{OFF} was recalculated before turning OFF the switch. If the disturbance were produced during the OFF period, it would take two switching cycles to reach the target point. The state-plane trajectories are given in Fig. 12(b) illustrating the similarity with the theoretical waveforms shown in Fig. 7.

Fig. 13(a) displays the transient response of the BCM NSS control law when $\alpha/\beta > 1$. This particular case was implemented by changing the reference impedance to $Z_r = 2\bar{Z}_o$ during the normalization process in the DSP code, which is equivalent to have $\alpha/\beta = 4$ and $\bar{L}_m/\bar{C}_o = 17.42$ if $n = 1/4$. From Fig. 13(a), the control performance worsens in comparison to the ideal case. At start-up conditions, it take several cycles to reach the target point as shown in the state-plane trajectories presented in Fig. 13(b). $I_{st\text{-}up}$ is calculated by replacing $\alpha/\beta = 1$ into (31) as 5.75 A, while the measured $I_{st\text{-}up}$ is 6.5 A. The measured start-up voltage V_x was 11 V while the calculated value using (33) when $\alpha/\beta = 4$ is 10.19 V. When a sudden load increase occurs, the target point will be lower than that one for the initial output current as noted in Fig. 8(d) which makes the output voltage dependable on the loading conditions. Fig. 14(a) presents the transient response of the BCM control

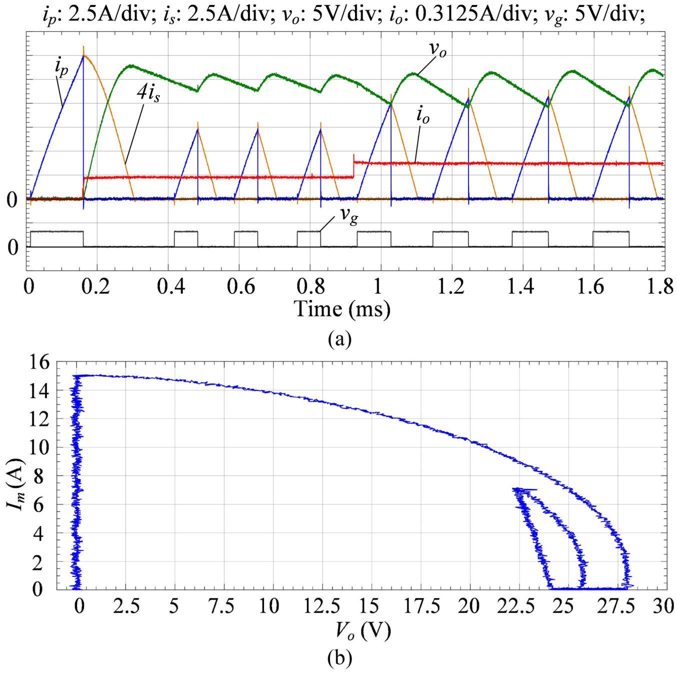

(a)

(b)

Fig. 14. (a) Transient response and (b) state-plane trajectory for the BCM NSS control law when $\alpha/\beta = 0.64$.

TABLE IV
SUMMARY RESULTS FOR THE BCM NSS CONTROL LAW

	Measured		Calculated		Error %	
	$I_{st\text{-}up}$	V_x	$I_{st\text{-}up}$	V_x	$I_{st\text{-}up}$	V_x
$\alpha/\beta = 1$	12.2 A	22.9V	11.5 A	23.3 V	4	1.04
$\alpha/\beta = 4$	6.5 A	11 V	5.7 A	10.2 V	11	7.36
$\alpha/\beta = 0.64$	15 A	28 V	14.4 A	28.1 V	4.1	0.21

law when $\alpha/\beta < 1$ which it is obtained by modifying the reference impedance $Z_r = 0.8\bar{Z}_o$ on the DSP code which compares to have $\alpha/\beta = 0.64$ and $\bar{L}_m/\bar{C}_o = 2.7870$. $I_{st\text{-}up}$ is measured as 15 A, while the calculated value from (31) was 14.38 A. The measured start-up voltage V_x is 28 V, while the calculated value from (33) when $\alpha/\beta = 0.64$ is 28.06 V. When $\alpha/\beta < 1$, L_m is overcharged. Therefore, the output overvoltage produces DCM operation since the control law does not allow Q to turn ON again until $v_o \leq V_{TP}$. The measured state-plane trajectories are shown in Fig. 14(b). The main results from the BCM NSS control law are summarized in Table IV.

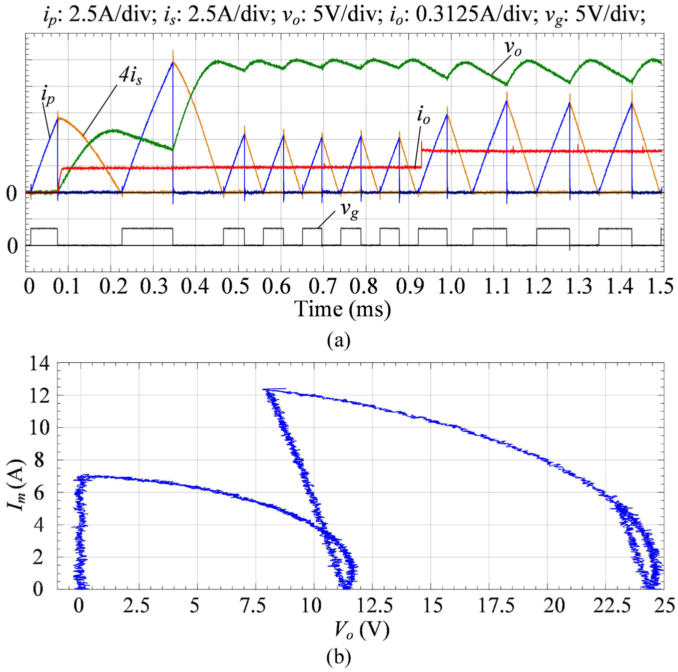

(a)

(b)

Fig. 15. (a) Transient response and (b) state-plane trajectory of the adaptive BCM NSS control law when $\alpha/\beta = 4$.

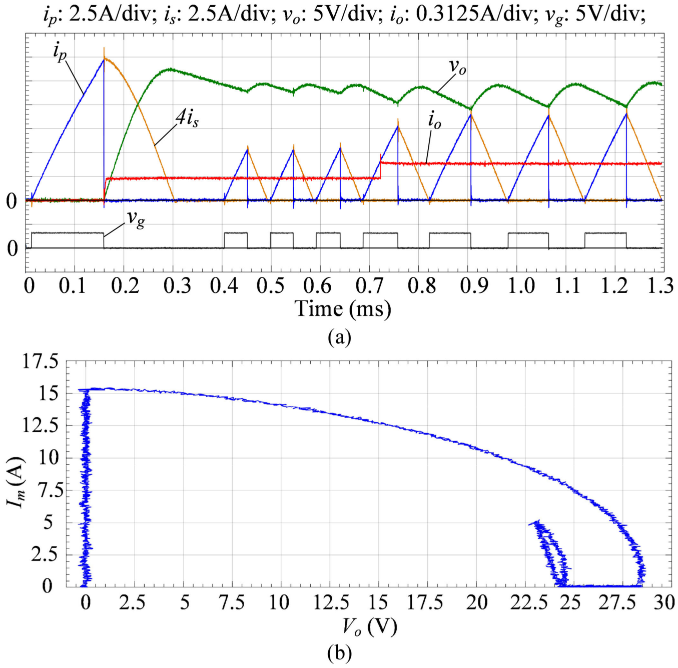

(a)

(b)

Fig. 16. (a) Transient response and (b) state-plane trajectory of the adaptive BCM NSS control law when $\alpha/\beta = 0.64$.

Fig. 15 presents the transient response and the state-plane trajectories when $\alpha/\beta = 4$ and the novel adaptive BCM NSS control law of Fig. 9 is implemented. From the start-up conditions, the converter is able to reach the target point in only two switching cycles as in the ideal case. Under a sudden load change, the converter is also able to reach V_{TP} in a single switching cycle. The start-up current $I_{st\text{-}up}$ is measured as 6.95 A which is higher than the value obtained using the non-adaptive BCM NSS control law since the computation time is higher in the adaptive case. The start-up voltage V_x is measured as 12.1 V, so the first estimation of α/β using (33) is 4.093 which represents a 2.325% error. The transient and the state-plane waveforms for the case where $\alpha/\beta = 0.64$ using the proposed adaptive controller are shown in Fig. 16. As in the previous case, the converter is able to reach the target point from start-up conditions in only two switching cycles but the flyback operates during the first switching cycle in DCM due to an initial output overvoltage. Using the measured start-up current and voltage $I_{st\text{-}up} = 14.75$ A and $V_x = 28$ V, the first estimation of $\alpha/\beta = 0.6685$ based on (33) which means a 4.45% of error. During steady-state operation when the sudden load change occurs, the adaptive BCM NSS controller is able

TABLE V
SUMMARY RESULTS FOR THE ADAPTIVE BCM NSS CONTROL LAW

	Measured		Calculated	Error %
	$I_{st\text{-}up}$	V_x	$(\alpha/\beta)_0$	$(\alpha/\beta)_0$
$\alpha/\beta = 1$	6.95 A	12.1 V	4.093	2.32
$\alpha/\beta = 0.64$	14.7 A	28 V	0.668	4.45

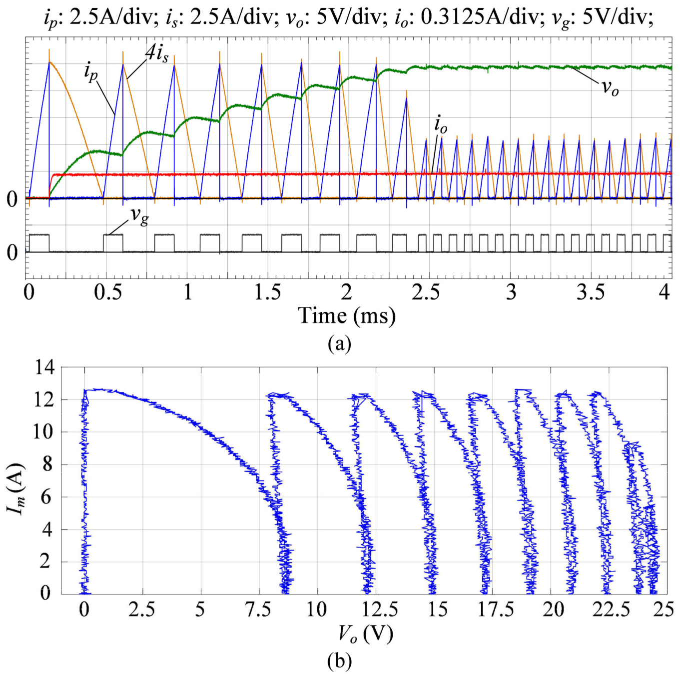

(a)

(b)

Fig. 17. (a) Transient response and (b) state-plane trajectory for the adaptive BCM NSS control law when the $I_{st\text{-}up}$ is limited to 12 A.

to reach the target point in one a single switching cycle as it occurs in the ideal case. The main results obtained from adaptive controller to make its first approximation to α/β are shown in Table V.

To illustrate a more realistic design where a low output voltage ripple is desired, Fig. 17 shows the experimental results for a case where C_o is increased to 61.28 μF, while keeping L_m as before. By replacing the converter parameters on (31), $I_{st\text{-}up} = 27.76$ A which is much higher than the value calculated in (59) for the parameters of Table I. For designs with low ripple and high-output voltage, $I_{st\text{-}up}$ may become many times greater than the steady-state magnetizing peak current. Therefore, it is necessary in those cases to limit the start-up current using (61). In the particular case of Fig. 17, $I_{max} = 12$ A was selected since the steady-state peak magnetizing current $I_{m,max}$ is 8 A from (60) when the load is at its maximum level. From Fig. 17, the ripple has decreased considerably with respect to previous experiments. A photograph of the experimental setup is provided in Fig. 18.

A. Comparison With a Linear PI Controller

To compare the new adaptive NSS controller with a standard linear controller under nominal and uncertain parameters, a linear controller was designed following the basic ideas from [8] and [9]. The performances of the linear controller and of the novel NSS controller are analyzed from experimental results where L_m and C_o are uncertain.

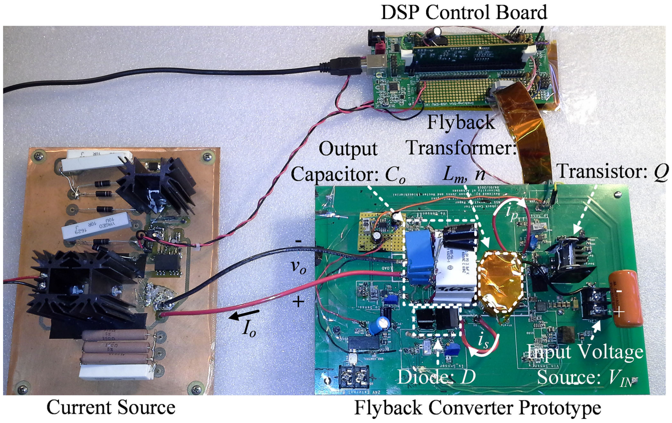

Fig. 18. Photograph of the experiment setup.

TABLE VI
EXPERIMENTAL PROTOTYPE PARAMETERS FOR COMPARISON WITH A LINEAR COMPENSATOR

Parameter	Value
N_p/N_s	1/4
L_m	45.8 μH
C_o	20.52 μF (film)

Spiazzi *et al.* [8], [9] present a linear control approach for a flyback converter operating in critical conduction mode with a resistive load. In those papers, the model of the converter is obtained by calculating the average current through the diode and then linearizing the expression of the output voltage around a desired operating point. Then, the linear compensator is designed.

Based on those references, an extension is made to the case of a flyback converter operating with a constant-current load. The necessary calculations to estimate the performance of the linear controller for the nominal plant and parameter uncertainties are presented in the Appendix including the step-by-step design procedure. Below, experimental results are presented. A summary of parameters of the nominal plant is presented in Table VI. The output capacitor is selected for the application to have high-output voltage ripple, so the figures can show clearly the waveform characteristics.

A digital approximation to the designed continuous-time PI controller was implemented in a DSP using a high sampling rate of 200 kHz for testing purposes. The implemented controller had two main purposes: 1) to produce BCM operation by measuring constantly the diode current, turning ON the transistor when the current reaches zero, and later turning OFF the transistor when the magnetizing current reaches the desired value $I_{m,pk}$; and 2) to measure the value of the output voltage and the reference voltage, evaluate the error signal and feed it to the PI compensator to evaluate the necessary $I_{m,pk}$ value which adjusts the output voltage.

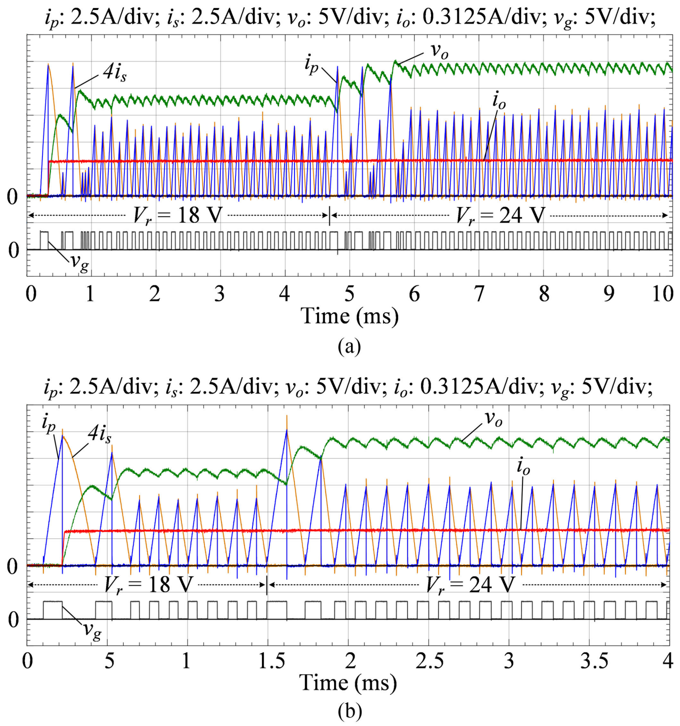

(a)

(b)

Fig. 19. Closed-loop response for a design with nominal plant parameters when $I_{st\text{-}up}$ is limited to 12 A for (a) a PI controller and (b) the novel adaptive NSS controller.

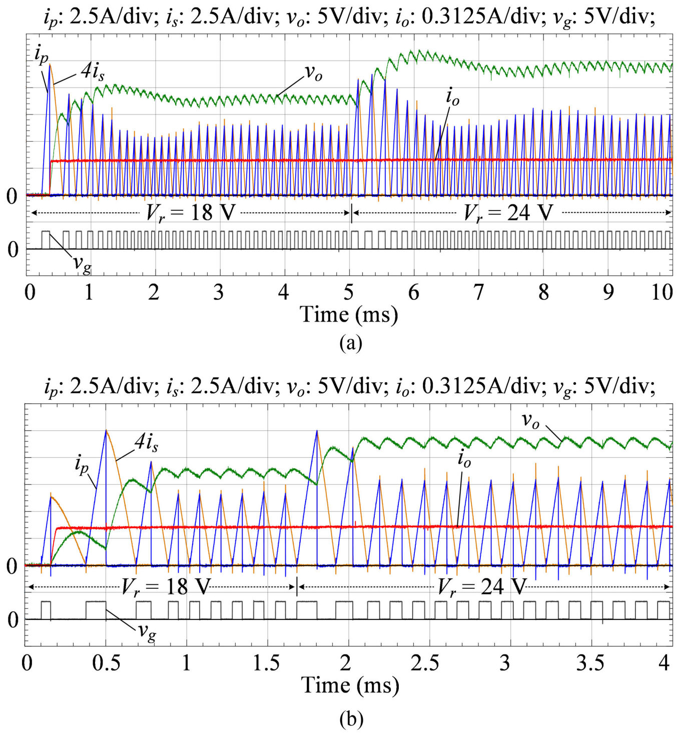

(a)

(b)

Fig. 20. Closed-loop response for a design with uncertain plant parameters ($\alpha/\beta = 4$) when $I_{st\text{-}up}$ is limited to 12 A for (a) a PI controller and (b) the novel adaptive NSS controller.

Three designs were made: The first one considering the plant with nominal parameters and the latter considering variations of the nominal values. The experimental tests were made all on the nominal plant where the implemented linear PI controller is designed on the basis of different perturbed plant parameters. Each case is compared with the corresponding adaptive NSS design. It is important to mention that the magnetizing current is limited to 12 A in all cases to avoid the saturation of the magnetic core (when the magnetizing current reaches 13.6 A, the value of the magnetizing inductance diminishes to 75% of the nominal value).

1) First Case. Nominal Design: A linear PI controller was designed for $\omega_n = 4681\ s^{-1}$, $\xi = 0.856$, leading to $K_i = 7280$, $K_p = 2.5$. Fig. 19(a) shows the performance of the experimental setup. Note the nonlinear effects of the saturation of the magnetizing current during startup as well as when applying a step change in the voltage reference at 4.693 ms from 18 to 24 V. The PI controller demands approximately 1.3 ms to reach the new steady-state condition performing 11 switching actions, while the novel adaptive NSS for the same conditions [see Fig. 19(b)] responds to the step change at 1.493 ms in approximately 0.4 ms performing two switching actions due to the limitation of the magnetizing current. If the magnetizing current was not limited and the core would not saturate, it would need just one switching cycle to reach the target output voltage.

2) Second Case. Design Based on Uncertain Parameters ($\alpha/\beta = 4$): In this experiment, the plant remains the same, but the design of the PI controller is made on the basis of uncertain plant parameters, considering $C_o = 5.13\ \mu$F. A linear PI controller was designed for $\omega_n = 4682.7\ \mathrm{s}^{-1}$, $\xi = 0.8387$, leading to $K_i = 1821.6$, $K_p = 0.4878$. Fig. 20(a) shows that the performance of the experimental setup is more oscillatory than the previous case due to the parametric variations and demands more than 3 ms (i.e., more than 22 switching actions) to reach a steady-state condition for a sudden change on the voltage reference V_r from 18 to 24 V occurring at 5.03 ms. As predicted by (A25), since $\beta < 1$, the response will be slower than in the ideal case. This case must be compared with Fig. 20(b) where the novel adaptive NSS controller is used and, despite the parametric error, the closed-loop response to the step change at 1.68 ms is very similar to the one obtained with the nominal design [see Fig. 19(b)].

3) Third Case. Design Based on Uncertain Parameters ($\alpha/\beta = 0.64$): The plant remains the same, but the design of the PI controller is made based on uncertain plant parameters, considering $C_o = 32.06\ \mu$F. A linear PI controller was designed for $\omega_n = 4683.2\ \mathrm{s}^{-1}$, $\xi = 0.8385$, leading to $K_i = 11387.2$, $K_p = 3.9131$. Fig. 21(a) shows the performance of the experimental setup. A rather unstable operation occurs during the first interval before the application of a step change in the output voltage reference from 18 to 24 V at time 3.952 ms. The output voltage waveform is noticeable worse than the obtained with the nominal design [see Fig. 19(a)]. The PI controller is reaching the new target point in about 1.3 ms after 13 switching actions. This case must be compared with Fig. 21(b) where the novel adaptive NSS controller shows almost the same response to the step change at 1.494 ms as for the nominal case despite the parametric variations, reaching a steady-state condition in two switching actions.

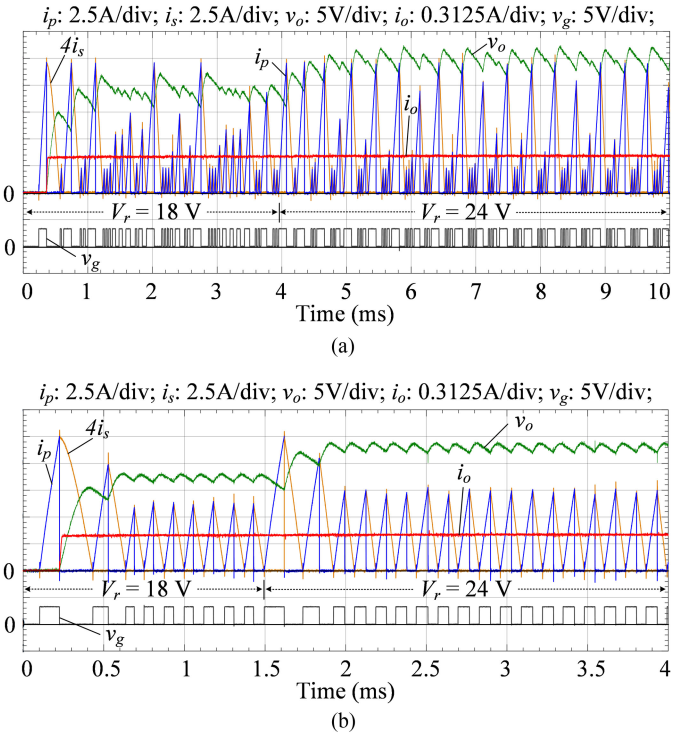

Fig. 21. Closed-loop response with uncertain plant parameters ($\alpha/\beta = 0.64$) when $I_{st\text{-}up}$ is limited to 12 A using (a) a PI controller and (b) the novel adaptive NSS controller.

VIII. CONCLUSION

The NSS for a flyback converter with parameter uncertainties operating in the BCM were obtained from the normalized converter differential equations. The derived nonlinear BC law brings the converter to the target point in a single switching cycle if the load does not change when the transistor Q is OFF during transient conditions. During start-up conditions where the load changes from zero to its rated value when the transistor is OFF, the worst-case scenario will be approaching the target point in only two switching cycles. During steady-state conditions, the controller will compensate for a sudden load change within only a single switching cycle.

The experimental results showed that for the nominal system ($\alpha/\beta = 1$, no parametric variations), the closed-loop response had no overshoot, zero steady-state error, and excellent response to sudden load changes. When parameter uncertainties were present ($\alpha/\beta \neq 1$), the performance of the typical NSS control degraded considerably due to the dependence of the normalized control trajectories to the converter parameters. To improve the system performance, an adaptive control scheme was implemented predicting the variation on the converter parameters by using the precisely derived converter natural trajectories. The controller made its first estimation of the parameter variations during the startup with a precision measured to be higher than 95%. Then, small adjustments were made cycle-by-cycle to adapt the control trajectories by measuring the error of the output voltage with respect to the target point producing a control response similar to the ideal case even under extreme parameter variations.

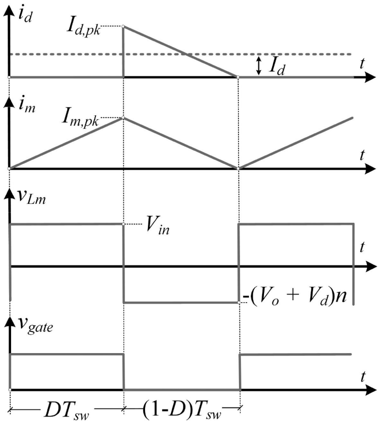

Fig. 22. Main waveforms for a flyback converter operating in BCM.

APPENDIX

The average current I_d through the diode in the secondary side of the transformer can be calculated from Fig. 22 as

$$I_d = \frac{I_{m,pk} n (1-D)}{2} = \frac{v_{in}}{L_m} D T_{sw} n \frac{(1-D)}{2} \tag{A1}$$

where D is the duty cycle which is calculated by analyzing the steady-state voltage waveform across the magnetizing inductance in BCM as

$$D = n (V_o + V_d) / (v_{in} + n (V_o + V_d)) \tag{A2}$$

where V_d is the voltage drop across the diode.

From (A1), I_d depends on the magnetizing inductance peak current $I_{m,pk}$. Therefore, $I_{m,pk}$ is used as the control variable to set the required average diode current [8], [9]. By replacing (A2) into (A1), I_d can be expressed as follows:

$$I_d = \frac{I_{m,pk}}{2} n \frac{v_{in}}{v_{in} + n (v_o + V_d)}. \tag{A3}$$

From (A3), I_d is a nonlinear function which depends on v_{in}, v_o, and $I_{m,pk}$. Linearizing (A3) around an operating point, $\hat{I}_d$ can be expressed by

$$\hat{I}_d = K_{in} \hat{V}_{in} + K_m \hat{I}_{m,pk} + K_o \hat{V}_o \tag{A4}$$

where K_{in}, K_m, and K_o are calculated by

$$K_{in} = \frac{\partial I_d}{\partial V_{in}} = \frac{I_{m,pk} n^2 (V_o + V_d)}{2(V_{in} + n (V_o + V_d))^2} \tag{A5}$$

$$K_m = \frac{\partial I_d}{\partial I_{m,pk}} = \frac{n V_{in}}{2 (V_{in} + n (V_o + V_d))} \tag{A6}$$

$$K_o = \frac{\partial I_d}{\partial V_o} = -\frac{n^2 V_{in} I_{m,pk}}{2(V_{in} + n (V_o + V_d))^2}. \tag{A7}$$

From the simplified flyback converter model shown in Fig. 23, the diode current in the Laplace s-domain can be expressed as follows:

$$\hat{i}_d (s) = \hat{i}_o (s) + s \bar{C}_o \hat{v}_o (s). \tag{A8}$$

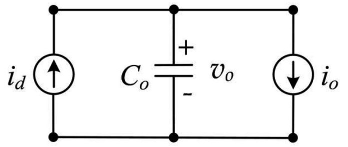

Fig. 23. Simplified averaged model of the flyback converter operating in BCM.

By combining (A4) and (A8), the following expression is obtained:

$$K_{in}\hat{V}_{in} + K_m \hat{I}_{m,pk} + K_o \hat{v}_o = \hat{i}_o\left(s\right) + s\bar{C}_o \hat{v}_o\left(s\right). \quad \text{(A9)}$$

To analyze the effect of $I_{m,pk}$ on $\hat{v}_o$, $\hat{V}_{in}$ and $\hat{i}_o$ are assumed to be zero in (A9). Then, the following transfer function is determined:

$$G\left(s\right) = \frac{v_o\left(s\right)}{I_{m,pk}\left(s\right)} = \frac{K_m/\bar{C}_o}{s - K_o/\bar{C}_o}. \quad \text{(A10)}$$

From (A7), K_o is negative so (A10) is a stable transfer function. As (A10) is based on an averaged model of the discontinuous diode current, it represents the averaged dynamics of the output voltage variations as a function of the variations of $I_{m,pk}$. Therefore, the model is valid for a frequency range whose upper limit is lower than the switching frequency of the flyback converter.

To evaluate the switching frequency, the ON- and OFF-time periods can be calculated from Fig. 22 as

$$\bar{T}_{ON} = \frac{I_{m,pk}\bar{L}_m}{V_{in}} \quad \text{(A11)}$$

$$\bar{T}_{OFF} = \frac{I_{m,pk}\bar{L}_m}{n\left(V_o + V_d\right)}. \quad \text{(A12)}$$

Then, the nominal switching frequency is calculated by

$$\bar{f}_{sw} = \frac{V_{in}\left(V_o + V_d\right)}{I_{m,pk}\bar{L}_m\left(V_o + V_d + V_{in}/n\right)} = \frac{V_{in}D}{I_{m,pk}\bar{L}_m}. \quad \text{(A13)}$$

Similarly, it can be done for the actual switching frequency

$$f_{sw} = \frac{V_{in}\left(V_o + V_d\right)}{I_{m,pk}L_m\left(V_o + V_d + V_{in}/n\right)} = \frac{V_{in}D}{I_{m,pk}L_m}. \quad \text{(A14)}$$

From the ratio between (A13) and (A14), the following relationship between f_{sw} and $\bar{f}_{sw}$ is obtained

$$\frac{f_{sw}}{\bar{f}_{sw}} = \frac{\bar{L}_m}{L_m} = \alpha. \quad \text{(A15)}$$

So, changes on the magnetizing inductance will produce switching frequency f_{sw} variations. The reference peak magnetizing current $I_{m,pk}$ used in the controller defines the steady-state output current level.

If a digital controller were to be designed to regulate the average output voltage of the plant (A10) by adjusting $I_{m,pk}$, it should use a sampling rate lower than the switching rate of the converter since the plant used for the design is an averaged model of the system. So, the minimum practical value of the switching frequency (A14), which occurs when V_{in} and D are minimum and L_m and $I_{m,pk}$ are maximum, would fix an upper limit to the closed-loop system bandwidth.

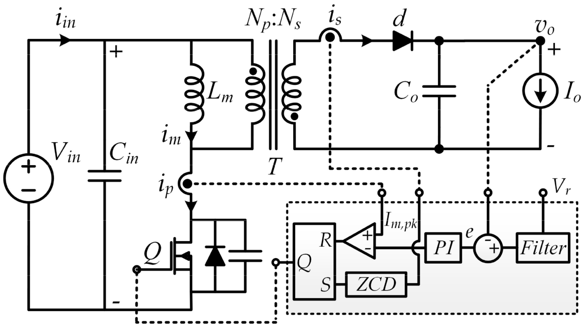

Fig. 24. Standard control strategy using a PI compensator [34], [35].

However, the following closed-loop transfer function is obtained if a continuous-time PI compensator is used to regulate the output voltage

$$\frac{v_o\left(s\right)}{v_r\left(s\right)} = \frac{\left(\bar{K}_p s + \bar{K}_i\right) K_m/\bar{C}_o}{s^2 + s\left(\bar{K}_p K_m - K_o\right)/\bar{C}_o + K_m\bar{K}_i/\bar{C}_o} \quad \text{(A16)}$$

where K_p and K_i are the proportional and integral gains of the PI controller.

If voltage V_r is pre-filtered as seen in Fig. 24, the zero in (A16) introduced by the compensator can be eliminated

$$\frac{v_o\left(s\right)}{v_r\left(s\right)} = \frac{\frac{\bar{K}_i}{\bar{K}_p}}{s + \frac{\bar{K}_i}{\bar{K}_p}} \frac{\left(\bar{K}_p s + \bar{K}_i\right)\frac{K_m}{\bar{C}_o}}{s^2 + s\frac{\left(\bar{K}_p K_m - K_o\right)}{\bar{C}_o} + \frac{K_m}{\bar{C}_o}\bar{K}_i}$$
$$= \frac{\bar{\omega}_n^2}{s^2 + 2\xi\bar{\omega}_n s + \bar{\omega}_n^2}. \quad \text{(A17)}$$

To guarantee that the model of (A10) is valid, the closed-loop dynamics should be selected to have its natural frequency at least ten times slower than the nominal operating switching frequency calculated from (A13). Therefore, the following identity should be established:

$$\bar{\omega}_n = \sqrt{\frac{K_m\bar{K}_i}{\bar{C}_o}} < \frac{1}{10}\bar{\omega}_{fsw} = \frac{1}{10}2\pi\bar{f}_{sw}. \quad \text{(A18)}$$

Then, K_i can be obtained as

$$\bar{K}_i < \left(\frac{1}{10}2\pi\bar{f}_{sw}\right)^2 \frac{\bar{C}_o}{K_m}. \quad \text{(A19)}$$

The proportional gain $\bar{K}_p$ can be designed by selecting the adequate damping ratio ξ for the closed-loop transfer function for the selected resonance frequency $\bar{\omega}_n = \sqrt{K_m\bar{K}_i/\bar{C}_o}$

$$\bar{K}_p = \left(2\xi\bar{\omega}_n\bar{C}_o + K_o\right)/K_m. \quad \text{(A20)}$$

If a PI compensator with nominal $\bar{K}_i$ and $\bar{K}_p$ is used to control a flyback converter with actual parameters C_o and L_m, the closed-loop transfer function pre-filtering V_r can be derived as follows:

$$\frac{v_o}{v_r} = \frac{\frac{\bar{K}_i}{\bar{K}_p}}{s + \frac{\bar{K}_i}{\bar{K}_p}} \frac{\frac{\left(\bar{K}_p s + \bar{K}_i\right)}{C_o}K_m}{s^2 + s\frac{\left(\bar{K}_p K_m - K_o\right)}{C_o} + \frac{K_m\bar{K}_i}{C_o}}. \quad \text{(A21)}$$

Therefore, the actual second-order parameters ξ and ω_n are given by

$$2\xi\omega_n = \bar{K}_p K_m / C_o - K_o / C_o \tag{A22}$$

$$\omega_n^2 = K_m \bar{K}_i / C_o. \tag{A23}$$

By substituting $\bar{K}_i$ and $\bar{K}_p$ by the maximum allowable value obtained from (A19) and (A20) into (A22) and (A23), the following relationships between the nominal and actual second-order time response parameters are obtained:

$$\xi = \bar{\xi}\sqrt{\beta} \tag{A24}$$

$$\omega_n = \bar{\omega}_n \sqrt{\beta} \tag{A25}$$

where β is the ratio between the nominal output capacitance $\bar{C}_o$ and the actual value C_o. Therefore, the parameter β will change the dynamic response of the controller. This continuous PI controller is implemented digitally by discretizing its dynamics at a high sampling rate of 200 kHz.

REFERENCES

[1] M. Kazimierczuk, *PulseWidth Modulated DC–DC Power Converters*, 1st ed. New York, NY, USA: Wiley, 2008.

[2] Q. Wu and Z. Zhu, “An adaptive high-precision OCP control scheme for flyback AC/DC converters,” *IEEE Trans. Power Electron.*, vol. 32, no. 12, pp. 8969–8973, Dec. 2017.

[3] C. Zhao, J. Zhang, and X. Wu, “An improved variable on-time control strategy for a CRM flyback PFC converter,” *IEEE Trans. Power Electron.*, vol. 32, no. 2, pp. 915–919, Feb. 2017.

[4] T. Yan, J. Xu, F. Zhang, J. Sha, and Z. Dong, “Variable-on-time-controlled critical-conduction-mode flyback PFC converter,” *IEEE Trans. Ind. Electron.*, vol. 61, no. 11, pp. 6091–6099, Nov. 2014.

[5] S. B. Kjaer, J. K. Pedersen, and F. Blaabjerg, “A review of single-phase grid-connected inverters for photovoltaic modules,” *IEEE Trans. Ind. Appl.*, vol. 41, no. 5, pp. 1292–1306, Sep./Oct. 2005.

[6] A. C. Kyritsis, E. C. Tatakis, and N. P. Papanikolaou, “Optimum design of the current-source flyback inverter for decentralized grid-connected photovoltaic systems,” *IEEE Trans. Energy Convers.*, vol. 23, no. 1, pp. 281–293, Mar. 2008.

[7] L. A. Garcia Rodriguez and J. C. Balda, “A comparison of isolated DC-DC converters for microinverter applications,” in *Proc. 28th Annu. IEEE Appl. Power Electron. Conf. Expo.*, Long Beach, CA, USA, 2013, pp. 2084–2091.

[8] G. Spiazzi, D. Tagliavia, and S. Spampinato, “DC-DC flyback converters in the critical conduction mode: a re-examination,” in *Proc. Conf. Rec. IEEE Ind. Appl. Conf. 35h IAS Annu. Meet. World Conf. Ind. Appl. Elect. Energy*, Rome, Italy, 2000, vol. 4, pp. 2426–2432.

[9] B. T. Irving, Y. Panov, and M. M. Jovanovic, “Small-signal model of variable-frequency flyback converter,” in *Proc. 18th Annu. IEEE Appl. Power Electron. Conf. Expo.*, Miami Beach, FL, USA, 2003, vol. 2, pp. 977–982.

[10] T. T. Song and H. S. h. Chung, “Boundary control of boost converters using state-energy plane,” *IEEE Trans. Power Electron.*, vol. 23, no. 2, pp. 551–563, Mar. 2008.

[11] J. M. Galvez, M. Ordonez, F. Luchino, and J. E. Quaicoe, “Improvements in boundary control of boost converters using the natural switching surface,” *IEEE Trans. Power Electron.*, vol. 26, no. 11, pp. 3367–3376, Nov. 2011.

[12] P. T. Krein, *Nonlinear Phenomena in Power Electronics: Attractors, Bifurcation, Chaos, and Nonlinear Control*. New York, NY, USA: IEEE Press, 2001, ch. 8.

[13] R. Munzert and P. T. Krein, “Issues in boundary control [of power convertors],” in *Proc. Rec. 27th Annu. IEEE Power Electron. Spec. Conf.*, Baveno, Italy, 1996, vol. 1, pp. 810–816.

[14] M. Greuel, R. Muyshondt, and P. T. Krein, “Design approaches to boundary controllers,” in *Proc. Rec. 28th Annu. IEEE Power Electron. Spec. Conf. Formerly Power Conditioning Spec. Conf., Power Process. Electron. Spec. Conf. 1972*, St. Louis, MO, USA, 1997, vol. 1, pp. 672–678.

[15] R. A. DeCarlo, S. H. Zak, and G. P. Matthews, “Variable structure control of nonlinear multivariable systems: a tutorial,” *Proc. IEEE*, vol. 76, no. 3, pp. 212–232, Mar. 1988.

[16] V. I. Utkin, “Sliding mode control design principles and applications to electric drives,” *IEEE Trans. Ind. Electron.*, vol. 40, no. 1, pp. 23–36, Feb. 1993.

[17] C. N. Onwuchekwa and A. Kwasinski, “Analysis of boundary control for buck converters with instantaneous constant-power loads,” *IEEE Trans. Power Electron.*, vol. 25, no. 8, pp. 2018–2032, Aug. 2010.

[18] K. K. S. Leung and H. S. H. Chung, “Derivation of a second-order switching surface in the boundary control of buck converters,” *IEEE Power Electron. Lett.*, vol. 2, no. 2, pp. 63–67, Jun. 2004.

[19] J. Y. C. Chiu, K. K. S. Leung, and H. S. H. Chung, “High-order switching surface in boundary control of inverters,” *IEEE Trans. Power Electron.*, vol. 22, no. 5, pp. 1753–1765, Sep. 2007.

[20] K. K. S. Leung and H. S. H. Chung, “A comparative study of boundary control with first- and second-order switching surfaces for buck converters operating in DCM,” *IEEE Trans. Power Electron.*, vol. 22, no. 4, pp. 1196–1209, Jul. 2007.

[21] W. T. Yan, C. N. M. Ho, H. S. H. Chung, and K. T. K. Au, “Fixed-frequency boundary control of buck converter with second-order switching surface,” *IEEE Trans. Power Electron.*, vol. 24, no. 9, pp. 2193–2201, Sep. 2009.

[22] P. K. W. Chan, H. Shu-Hung Chung, and S. Y. Hui, “A generalized theory of boundary control for a single-phase multilevel inverter using second-order switching surface,” *IEEE Trans. Power Electron.*, vol. 24, no. 10, pp. 2298–2313, Oct. 2009.

[23] Y. He, H. S. H. Chung, C. N. M. Ho, and W. Wu, “Use of boundary control with second-order switching surface to reduce the system order for deadbeat controller in grid-connected inverter,” *IEEE Trans. Power Electron.*, vol. 31, no. 3, pp. 2638–2653, Mar. 2016.

[24] Y. He, H. S. H. Chung, C. N. M. Ho, and W. Wu, “Direct current tracking using boundary control with second-order switching surface for three-phase three-wire grid-connected inverter,” *IEEE Trans. Power Electron.*, vol. 32, no. 7, pp. 5723–5740, Jul. 2017.

[25] T. Messikh, N. Rahim, and M. Saad, “Boundary control of dual-output boost converter using state-energy plane,” *IET Power Electron.*, vol. 7, no. 9, pp. 2310–2321, Sep. 2014.

[26] S. Chen, Y. M. Lai, S. C. Tan, and C. K. Tse, “Boundary control with ripple-derived switching surface for DC–AC inverters,” *IEEE Trans. Power Electron.*, vol. 24, no. 12, pp. 2873–2885, Dec. 2009.

[27] M. Ordonez, M. T. Iqbal, and J. E. Quaicoe, “Selection of a curved switching surface for buck converters,” *IEEE Trans. Power Electron.*, vol. 21, no. 4, pp. 1148–1153, Jul. 2006.

[28] M. Ordonez, J. E. Quaicoe, and M. T. Iqbal, “Advanced boundary control of inverters using the natural switching surface: Normalized geometrical derivation,” *IEEE Trans. Power Electron.*, vol. 23, no. 6, pp. 2915–2930, Nov. 2008.

[29] J. M. Galvez and M. Ordonez, “High performance boundary control of boost-derived PFCs: Natural switching surface derivation and properties,” *IEEE Trans. Power Electron.*, vol. 27, no. 8, pp. 3807–3816, Aug. 2012.

[30] J. M. Galvez, M. Ordonez, T. T. Nguyen, and F. Luchino, “Boundary control of buck-boost converters: Normalized trajectories and the natural switching surface,” in *Proc. IEEE Energy Convers. Congr. Expo.*, Raleigh, NC, USA, 2012, pp. 358–363.

[31] G. G. Oggier, M. Ordonez, J. M. Galvez, and F. Luchino, “Fast transient boundary control and steady-state operation of the dual active bridge converter using the natural switching surface,” *IEEE Trans. Power Electron.*, vol. 29, no. 2, pp. 946–957, Feb. 2014.

[32] G. G. Oggier and M. Ordonez, “Boundary Control of Full-bridge ZVS: Natural switching surface for transient and steady-state operation,” *IEEE Trans. Ind. Electron.*, vol. 61, no. 2, pp. 969–979, Feb. 2014.

[33] L. A. Garcia-Rodriguez, E. Williams, J. C. Balda, J. Gonzalez-Llorente, and H. Chiacchiarini, “Control of a flyback converter operating in BCM using the natural switching surface,” in *Proc. IEEE 6th Int. Symp. Power Electron. Distrib. Gener. Syst.*, Aachen, Germany, 2015, pp. 1–8.

[34] L. A. G. Rodriguez, H. Chiacchiarini, and J. C. Balda, “Control of a flyback converter with parametric uncertainties operating in BCM Using the natural switching surface,” in *Proc. IEEE Biennial Congr. Argentina*, Buenos Aires, Argentina, 2016, pp. 1–7.

[35] E. O. Lindstrom, L. A. Garcia-Rodriguez, A. R. Oliva, and J. C. Balda, “Designing an optimum non-dissipative LC snubber for step-up flyback converters in DCM,” in *Proc. IEEE 8th Latin Amer. Symp. Circuits Syst.*, Bariloche, Argentina, 2017, pp. 1–4.

Luciano Andrés Garcia Rodriguez (S'12) received the B.S. degree in electronics engineering from the Universidad Nacional del Sur, Bahía Blanca, Argentina. He is currently working toward the Ph.D. degree in electrical engineering with the University of Arkansas, Fayetteville, AR, USA.

He has been a Research and Teaching Assistant with the University of Arkansas. His current research interests include novel topologies for power electronics converters, high-frequency and high-power transformer designs, and novel non-linear adaptive control schemes.

Héctor Gerardo Chiacchiarini was born in Villa Regina, Argentina, in 1964. He received the B.Sc. degree in electronics engineering and the Ph.D. degree in control systems from the Universidad Nacional del Sur (UNS), Bahía Blanca, Argentina, in 1990 and 1996, respectively.

In 2001, he was a Visiting Scholar with the ETH Zurich, Switzerland, and in 2004, with the University of Arkansas, USA. He is currently a Professor with the Departamento de Ingeniería Eléctrica y de Computadoras, Universidad Nacional del Sur, teaching power electronics and industrial robotics. Since 1999, he has also been a Researcher with the Instituto de Investigaciones en Ingeniería Eléctrica "Alfredo Desages," UNS-CONICET. He has coauthored more than 110 works published in journals, book chapters, and conferences. He has participated in more than 30 research projects being the Director of 13 of them. His main research interests include power electronics, robotics, mechatronics, motor drives, control systems, and applications in energy storage and power management.

David Carballo Rojas (S'14) was born in Santiago, Panama, in 1993. He received the B.S. degree in electrical engineering from the University of Arkansas, Fayetteville, AR, USA, in 2016, where he is currently working toward the M.S. degree with the Department of Electrical Engineering under the supervision of Dr. J. C. Balda.

His current research interests include power electronics, stability of grid-connected power electronics, and power quality.

Juan Carlos Balda (M'78–SM'94) received the B.Sc. degree in electrical engineering from the Universidad Nacional del Sur, Bahía Blanca, Argentina, in 1979, and the Ph.D. degree in electrical engineering from the University of Natal, Durban, South Africa, in 1986.

He was a Researcher and a part-time Lecturer with the University of Natal until 1987. He was a Visiting Assistant Professor with Clemson University, Clemson, SC, USA, for two years. He has been with the University of Arkansas, Fayetteville, AR, USA, since 1989, where he is currently a University Professor, a Department Head, and an Associate Director of Applications with the National Center for Reliable Electric Power Transmission and a Campus Director with the NSF IUCRC Grid-Connected Advanced Power Electronic Systems. His current research interests include power electronics, electric power distribution systems, motor drives, and electric power quality.

Dr. Balda is a member of the honor society Eta Kappa Nu. He is also the Vice-Chair of the IEEE Power Electronics Society (PELS) TC5 Committee and a Faculty Advisor of the local chapter of the IEEE PELS.